

A linear theory of extratropical synoptic eddy statistics

Jeffrey S. Whitaker and Prashant D. Sardeshmukh

*Cooperative Institute for Research in the Environmental Sciences (CIRES),
University of Colorado, Boulder, Colorado*

submitted *J. Atmos Sci*

May 2, 1996

Abstract

This paper investigates the extent to which extratropical synoptic eddies may be viewed as stochastically forced disturbances evolving on a baroclinically stable planetary scale background flow. To this end, a two-level hemispheric quasi-geostrophic model is linearized about the observed long-term mean flow and forced with Gaussian white noise. The mean flow is shown to be exponentially stable for a reasonable choice of dissipation parameters. Synoptic-scale eddy disturbances can still grow on such a flow, albeit for a finite time, either in response to the stochastic forcing or through local energy interactions with the basic state. In a statistically steady state, a fluctuation dissipation relation (FDR) links the covariance structure of the eddies to the spatial structure of the basic state and the covariance structure of the forcing. If the forcing is assumed to have a trivial statistical structure, i.e. white in both space and time, the FDR amounts to an unambiguous one-to-one relationship between the spatial structure of the basic state and the covariance structure of the eddies, and therefore constitutes a theory of the eddy statistics. The theory is complete in the sense that for any given background flow, it predicts all of the second-order eddy statistics, such as eddy kinetic energy, momentum and heat fluxes, and spectra. It is also self-consistent in that it neither admits nor predicts higher order statistics. Despite the drastic assumptions made, the comparisons of the predicted and observed geographical distributions of eddy kinetic energy, momentum and heat fluxes are found to be extremely encouraging. The theory is also shown to be sensitive enough to basic state changes that it is able to capture important aspects of observed storm track variability associated with seasonal and interannual changes in the background flow.

1. Introduction.

The last two decades have seen considerable progress in the modeling and prediction of extratropical weather systems. Numerical weather prediction models are now able to forecast them up to nearly a week ahead of time, and many general circulation models (GCMs) are able to capture important aspects of their general behavior as represented in variance and covariance statistics. Parallel advances have also been made in the understanding of their dynamics in a variety of situations, aided in significant measure by "potential vorticity thinking".

Despite these advances, however, a successful theory of the statistics of such eddies has yet to emerge. By itself, a reasonable simulation of the eddy statistics in GCMs does not constitute such a theory. Without a theory one cannot understand why, for example, a GCM produces synoptic eddy variance maxima where it does or why it does not produce variance maxima where it should. A quantitative theory of the eddy statistics would help one understand such model deficiencies. It would also help one understand better the geographical distributions of the observed climatological mean synoptic eddy variances and fluxes, their changes from season to season, from year to year, and during persistent extreme anomaly events.

A theory of the eddy statistics should link the statistics of the eddies to the structure of the background flow. Synoptic eddies have almost always been discussed in relation to a background flow, either steady, time-mean, slowly evolving, or representative of some 'instantaneous' weather regime. When the focus shifts from the behavior of individual eddies to that of an ensemble of eddies, consideration of the ensemble average flow as a background flow becomes even more relevant. Nevertheless, as is well recognized, such a separation of the total flow into mean and eddy parts often causes conceptual difficulties, and also raises the issue of to what extent the mean flow actually *determines* the eddy statistics or vice versa. Regardless of cause and effect, however, one can still always ask the question: Given an ensemble-average flow, to what extent can one deduce the ensemble-average eddy statistics? This is the problem considered in this paper.

In this paper, the term 'synoptic eddy statistics' will be used to denote the covariance and lag-covariance statistics of eddies with periods between 1 and 8 days. To fix ideas, consider the evolution equation for such eddies in the form

$$\frac{d\tilde{\mathbf{x}}}{dt} = \mathbf{L}\tilde{\mathbf{x}} + \tilde{\mathbf{n}} + \tilde{\mathbf{F}}, \quad (1)$$

where $\tilde{\mathbf{x}}$ is the vector of eddy expansion coefficients in say a spherical harmonic basis, \mathbf{L} is a linear operator in that basis, $\tilde{\mathbf{n}}$ denotes nonlinear terms and $\tilde{\mathbf{F}}$ represents forcing. We will assume that (1) has been written in such a way that $\tilde{\mathbf{x}}$ is a real vector and \mathbf{L} is a real matrix. Note that $\mathbf{L}\tilde{\mathbf{x}}$ includes eddy dissipation terms in addition to the terms linearized about a specified background flow. Our aim in this paper is to relate the covariance matrices

$$\mathbf{C}_0 = \langle \tilde{\mathbf{x}}(t)\tilde{\mathbf{x}}^T(t) \rangle, \quad (2a)$$

$$\mathbf{C}_\tau = \langle \tilde{\mathbf{x}}(t+\tau)\tilde{\mathbf{x}}^T(t) \rangle \quad (2b)$$

of the synoptic eddies, where angle brackets $\langle \rangle$ denote an ensemble average (which is often estimated as a time average) to the structure of the background flow. To this end, we will approximate the sum of the nonlinear and forcing terms in (1) as

$$\tilde{\mathbf{n}} + \tilde{\mathbf{F}} = \mathbf{D}\tilde{\mathbf{x}} + \tilde{\mathbf{F}}_s, \quad (3)$$

where $\tilde{\mathbf{F}}_s$ is Gaussian white noise. This represents a slight generalization of an approximation often made in linear theories of classical turbulence in which the nonlinear terms are hypothesized to have two major effects: equilibration and excitation. Eq. (3) is only expected to hold on average, not for every realization; one may think of it as a linear regression approximation. With this approximation (1) becomes

$$\frac{d\tilde{\mathbf{x}}}{dt} = (\mathbf{L} + \mathbf{D})\tilde{\mathbf{x}} + \tilde{\mathbf{F}}_s = \mathbf{B}\tilde{\mathbf{x}} + \tilde{\mathbf{F}}_s. \quad (4)$$

We will specify \mathbf{D} such that \mathbf{B} is a stable operator, i.e. all its eigenvalues have negative real parts. Equation (4) then becomes a multivariate linear Markov model of the synoptic eddies.

The general properties of a model such as (4) have been discussed recently in detail in other geophysical contexts by DelSole and Farrell (1995), Penland and Sardeshmukh (1995) and Newman, Sardeshmukh and Penland (1996; hereafter NSP). Its most important property is that without forcing, all eddies eventually decay. In a multivariate system, however, that decay need not be monotonic. If the maximum singular value of the operator $\exp(\mathbf{B}\tau)$ is greater than 1 for some τ , then eddy growth is possible over the interval $[t, t+\tau]$. Nevertheless, to achieve a statistically stationary state, the general decaying tendency of the eddies must be balanced by forcing. This balance condition, known in the stochastic dynamical systems literature as a fluctuation-dissipation relation (FDR; see Penland and Matrosova 1994) may be expressed as

$$\mathbf{B}\mathbf{C}_0 + \mathbf{C}_0\mathbf{B}^T + \mathbf{Q} = 0, \quad (5)$$

where $\mathbf{Q} = \left\langle \tilde{\mathbf{F}}_s(t)\tilde{\mathbf{F}}_s^T(t) \right\rangle dt$ is the covariance matrix of the stochastic white noise forcing. Note that \mathbf{Q} is symmetric but not necessarily diagonal, i.e. $\tilde{\mathbf{F}}_s$ is white in time but not necessarily white in space. Equation (5) links the covariance structure of the eddies, \mathbf{C}_0 , to the structure of the background flow, \mathbf{B} , and to the structure of the forcing, \mathbf{Q} . Given \mathbf{B} and \mathbf{Q} , therefore, one can solve for \mathbf{C}_0 . The lag-covariance matrices \mathbf{C}_τ are related to \mathbf{C}_0 in any dynamical system of the form (4) as

$$\mathbf{C}_\tau = \exp(\mathbf{B}\tau)\mathbf{C}_0 \quad (\tau > 0), \quad (6)$$

and can therefore also be determined once \mathbf{C}_0 is known.

To simplify even further, we hypothesize that the geographical coherence of the forcing is unimportant in (5), and approximate \mathbf{Q} as $\mathbf{Q} = \varepsilon \mathbf{I}$, where \mathbf{I} is the identity matrix and ε is a scaling constant. Our parameterization of the eddy statistics then becomes

$$\mathbf{B}\mathbf{C}_0 + \mathbf{C}_0\mathbf{B}^T + \varepsilon\mathbf{I} = 0, \text{ and} \quad (7a)$$

$$\mathbf{C}_{\tau>0} = \exp(\mathbf{B}\tau)\mathbf{C}_0, \quad (7b)$$

$$\mathbf{C}_{\tau<0} = \mathbf{C}_{\tau>0}^T. \quad (7c)$$

Given any background flow, i.e. \mathbf{B} , we determine \mathbf{C}_0 through (7a) and \mathbf{C}_τ through (7b). Note that (7a) implies that *if the background flow changes, the eddy statistics change in such a way that the symmetric part of $\mathbf{B}\mathbf{C}_0$ remains invariant*. This is the essence of our parameterization. Note that the prediction of a *change* in \mathbf{C}_0 does not depend upon an explicit specification of \mathbf{Q} . We only need \mathbf{Q} to predict the actual \mathbf{C}_0 , and will show below that specifying $\mathbf{Q} = \varepsilon\mathbf{I}$, works quite well.

If $\tilde{\mathbf{x}}_\omega$ is the Fourier transform of the multivariate Markov process $\tilde{\mathbf{x}}(t)$ in (4), then its covariance matrix in the frequency domain is

$$\mathbf{C}_\omega \equiv \langle \tilde{\mathbf{x}}_\omega \tilde{\mathbf{x}}_\omega^{T*} \rangle = (\omega\mathbf{I} + i\mathbf{B})^{-1} \mathbf{Q} (\omega\mathbf{I} - i\mathbf{B}^T)^{-1}, \quad (8)$$

where (T^*) denotes complex-conjugate transpose. The power spectra of all components of $\tilde{\mathbf{x}}_\omega$, as well as their cross-spectra, are given by (8). \mathbf{C}_ω and \mathbf{C}_τ form a Fourier transform pair,

$$\mathbf{C}_\tau = \frac{1}{2\pi} \int_{-\infty}^{+\infty} \mathbf{C}_\omega e^{-i\omega\tau} d\omega, \quad (9a)$$

$$\mathbf{C}_\omega = \int_{-\infty}^{+\infty} \mathbf{C}_\tau e^{i\omega\tau} d\tau. \quad (9b)$$

Thus the solution of (7), for all τ , yields not only complete information on the spatial structure of the eddies, but their Fourier spectra as well.

Some caveats are in order. The parameterization problem is meaningfully posed only for ensembles that include a sufficiently large number of synoptic eddy events that their statistics can be reliably defined. For ensemble averages defined as time averages, this suggests that one should probably consider averages over at least one, and preferably many, 90-day seasons. We will consider the problems of deducing the 13-winter (DJF) average eddy statistics for 1982-95 given the 13-winter average flow, the differences between the 13 year average eddy statistics for mid-winter (January) and mid-spring (April) given the differences between the 13-year mean flows for these months, and finally, the anomalous eddy statistics for individual winters, given the anomalous flows for those winters. From sampling considerations alone, one would expect some degradation in the answers to these problems as the sample size is reduced.

There is however another, and perhaps even more important, reason as to why one should expect a degradation in the answers for smaller sample sizes. Any parameterization problem is well posed only to the extent that there is a clear scale separation between the eddies and the mean flow, i.e. a clear spectral gap. We define our synoptic eddies as eddies with timescales shorter than 8 days, and our mean flow as flow with timescales longer than 90 days. It might therefore appear that we have adequate scale separation. It is however important to bear in mind that there is actually no spectral gap in the observations. The spectrum of the observed variability is predominantly red, and eddies with timescales between 10 and 90 days may also be expected to affect the synoptic eddy statistics. One could thus observe, in principle, different 90-day mean eddy statistics associated with the same 90-day mean flow. Since the intermediate timescale eddies are unaccounted for in our analysis, they contribute in effect an unparameterizable portion to the synoptic eddy covariances in our problem. One could reasonably expect this contribution to be smaller for larger ensembles (such as climate means), particularly if it is a linear function of the intermediate timescale eddies. For individual winters, however, it could be relatively large, and remains to be determined.

Our linear model \mathbf{L} in (1) will be a two-level, hemispheric, linear balance model linearized about representative observed zonally varying flows at 400 and 800 mb. We will specify \mathbf{D} in (4)

as a simple linear drag. The scaling constant ϵ in (7) will be chosen so that the eddy kinetic energy obtained via (7) matches observations. Maps of the eddy streamfunction variance, kinetic energy, vorticity and heat fluxes predicted by (7) will be compared with the corresponding observed quantities.

To the extent that our parameterization of the eddy statistics is successful, one could claim that *on average*, synoptic eddy evolution is governed by (4), where \mathbf{B} is a stable linear operator. This should not however necessarily be taken to imply that the atmosphere is baroclinically stable. We claim only that $\mathbf{B} = \mathbf{L} + \mathbf{D}$ is stable, not \mathbf{L} . As discussed above, \mathbf{D} could be viewed as a linear approximation to the damping effects of quadratic nonlinearities. Nevertheless, it turns out that our \mathbf{L} operator, by itself, is only marginally unstable for all of the background flows considered here, so specifying \mathbf{D} as a simple weak damping with a time scale of 10 days is enough to stabilize \mathbf{B} . This weak extra damping \mathbf{D} is arguably within the range of uncertainty of the damping that should ideally be specified in a two-level model. In any event, the implication is that *one need not invoke normal mode baroclinic instability to explain most features of the second-order statistics of observed synoptic systems*. Predictions of individual realizations, i.e. individual weather forecasts, are another matter, although even here it will be shown that (4) performs much better than persistence over 5 days and has comparable skill to that of current operational model forecasts over 2 days.

Finally, we stress again that even if \mathbf{B} is a stable operator, this does not imply that all eddy growth is associated with the stochastic forcing. As mentioned above, if $\exp(\mathbf{B}\tau)$ has singular values greater than 1, as is true in our system, then eddy growth is possible over any interval $[t, t+\tau]$. Note that the energy for this growth comes from the background flow, not the forcing. Indeed we will make a case that nearly 75% of the domain integrated eddy variance in the statistically equilibrated system (4) comes from the background flow, and only about 25% from the stochastic forcing. Locally, in the jet regions where the energy source associated with shears in the background flow is strongest, the relative importance of the energy source associated with the stochastic driving is even less.

The paper is organized as follows. Section 2 describes the observational datasets and data filtering procedures, the two-level model equations, and the procedure for solving (7) for \mathbf{C}_0 and \mathbf{C}_τ . Results for the climatological mean winter eddy statistics are presented in section 3. The simulations of the seasonal and interannual variations of the statistics are presented in section 4. Sensitivity of the results to the specification of the extra damping \mathbf{D} in (4) is discussed in section 5. Section 5 also considers the sensitivity of the results to the norm in which \mathbf{Q} is approximated as $\epsilon \mathbf{I}$ (i.e whether all spatial scales of streamfunction, kinetic energy or vorticity are excited equally by the stochastic forcing). Finally, section 6 follows with a discussion and conclusions.

2. Data, equations and solution procedure.

2.1 Observational data and processing.

The data used in this study were derived from the National Centers for Environmental Prediction (NCEP) reanalysis dataset (Kalnay et al, 1996). We utilize global 400, 700, and 850 mb wind fields sampled four times daily for the period 1982-1995. Winds at the 800 mb level were estimated by linear interpolation in the natural logarithm of pressure between 700 and 850 mb. Spherical harmonic coefficients of the 400 and 800 mb angular velocity (winds multiplied by cosine of latitude) were then calculated from the 2.5° gridded data using the SPHEREPACK¹ package (Swartztrauber, 1984), and these coefficients were truncated to T31 resolution. Only the nondivergent winds were used in the analysis; these were obtained from the spectral coefficients of the vorticity field. High frequency filtered data were obtained by applying a 251 point 1-8 day bandpass Lanczos filter to the 400 and 800 mb streamfunction coefficient time series.

2.2 The two-level model.

¹FORTTRAN source code available free from the National Center for Atmospheric Research (NCAR) via anonymous ftp (ftp.ucar.edu).

We use a quasi-geostrophic two-level model based on the linear balance equation (Lorenz 1960, Frederiksen 1983, often referred to as the "P-model"). After nondimensionalizing using the radius of the earth (a) as a length scale and the inverse of the earth's rotation rate (Ω^{-1}) as a time scale, the governing equations may be written;

$$\frac{\partial}{\partial t} \nabla^2 \psi_j + J(\psi_j, \nabla^2 \psi_j + 2\mu) + \nabla \cdot 2\mu \nabla \chi_j = -\left((2-j)r_M + \nu \nabla^4\right) \nabla^2 \psi_j, \quad (10)$$

$$\frac{\partial}{\partial t} (\phi_2 - \phi_1) + \frac{1}{2} J(\psi_2 + \psi_1, \phi_2 - \phi_1) + \sigma \omega_{3/2} = -\left(r_T + \nu \nabla^4\right) (\phi_2 - \phi_1), \quad (11)$$

$$\nabla^2 (\phi_2 - \phi_1) = \nabla \cdot 2\mu \nabla (\psi_2 - \psi_1), \quad (12)$$

where $J(A,B) \equiv \frac{\partial A}{\partial \mu} \frac{\partial B}{\partial \lambda} - \frac{\partial B}{\partial \mu} \frac{\partial A}{\partial \lambda}$, ψ is streamfunction, ϕ is geopotential, χ is velocity potential, μ is the sine of latitude, $\omega \equiv dp/dt$, and (r_M , r_T , ν) are damping parameters. The subscript $j=1(2)$ denotes the 800 mb (400 mb) level, while the subscript $3/2$ denotes the 600 mb level. The variables ψ , χ , ϕ and ω are nondimensionalized by Ωa^2 , $(\Omega a)^2$, $(\Omega a)^2$ and $\Omega \Delta p$, respectively, where $\Delta p = p_2 - p_1 = -400$ mb. The static stability parameter σ is assumed to be a constant, given by

$$\sigma \equiv \frac{-\Delta \pi \Delta \Theta}{\Omega^2 a^2} \quad (13)$$

where $\Delta \pi$ is the difference between the Exner function ($\equiv c_p (p/p_0)^{R/c_p}$) at 400 and 800 mb and $\Delta \Theta$ is the mean potential temperature difference between 400 and 800 mb. For all of the results presented here, the dimensional values of the lower level Rayleigh damping (r_M), the thermal damping (r_T) and the coefficient of the biharmonic diffusion (ν) are fixed at $2/5 \text{ d}^{-1}$, $1/7 \text{ d}^{-1}$ and $2.338 \times 10^{16} \text{ m}^4 \text{ s}^{-1}$, respectively. The static stability parameter is fixed by specifying $\Delta \Theta = 15 \text{ K}$.

The horizontal boundary conditions are

$$\omega_{5/2} = 0 \text{ and } \omega_{1/2} = J(\psi_1, h), \quad (14)$$

where h is topographic height (scaled by $\rho_o g / \Delta p$, where ρ_o is a reference value of density at 1000 mb) and the subscript 1/2 (5/2) denotes the 1000 mb (200 mb) level. The velocity potential χ is related to ω through the continuity equation

$$\nabla^2 \chi_j = (2j - 3)\omega_{3/2} + (2 - j)\omega_{1/2} \quad (15)$$

The vorticity equation (10) is the prognostic equation for the model. Since geopotential and streamfunction are coupled through the balance equation (12), elimination of the time derivatives in (10) and (11) using $\partial/\partial t$ of (12) yields a diagnostic " ω -equation" for the divergent flow (not shown).

2.3 Calculation of eddy statistics.

The linearized version of the two-level model described above may be used to construct \mathbf{L} , the matrix representing the linearized dynamical operator. Here we use the observed nondivergent seasonally averaged flow at 400 and 800 mb to determine the basic state, while the static stability σ and the damping coefficients (r_M, r_T, ν) are fixed to the values given previously.

The operator \mathbf{D} in (4) is chosen to be a linear damping on the state variables (so that it may be incorporated into the model without changing the eigenvectors or the imaginary parts of the eigenvalues of \mathbf{L}) by simply shifting the real parts of the eigenvalues by an amount equal to the damping rate. Unless otherwise noted, this damping rate is set to $1/10 \text{ days}^{-1}$, which is more than sufficient to stabilize $\mathbf{L} + \mathbf{D}$ for observed long-term seasonal mean basic states. Further discussion of the sensitivity of our results to \mathbf{D} is given in section 5.

Approximating $\tilde{\mathbf{F}}_s$ in (4) as geographically incoherent white noise yields (7), our model of the eddy statistics. The stochastic term represents the combined effects of eddy excitation due to

random fluctuations in the nonlinear interactions and forcing. As discussed in the introduction, our view is that to the extent that our parameterization (7) is useful, the eddy dynamics must be primarily governed by \mathbf{L} , and not be very sensitive to the exact form of $\tilde{\mathbf{F}}_s$. From this perspective, the role of $\tilde{\mathbf{F}}_s$ is simply to provide some eddy excitation. The horizontal and vertical shears in the basic flow then act to control the spatial structure and propagation characteristics of the eddies.

To the extent that; 1) \mathbf{L} is a good model for the linear dynamical evolution of high-frequency transients, 2) nonlinearity and forcing play secondary roles in governing the *statistics* of the eddies and hence may be crudely approximated as white noise plus a linear damping, and 3) $\mathbf{L} + \mathbf{D} = \mathbf{B}$ is stable, equations (7) represent a complete theory for the statistics of storm track eddies. The theory is complete in the sense that once \mathbf{B} is defined, all of the second order statistics of the eddies, as well as their Fourier spectra, are known from (7) and (9).

2d. Solution procedure.

The spherical harmonic expansion of the state variable is truncated at T31, yielding a 2048 element real state vector in (4). To further reduce the dimensionality, we reflect the Northern Hemisphere basic state onto the Southern Hemisphere, and also impose hemispheric symmetry on the eddies. This results in an \mathbf{L} of rank 992. To prevent the development of spurious equatorially trapped disturbances, an equatorial sponge zone with a \cos^{48} latitudinal dependence and a decay time scale of 5 days at the equator is included in \mathbf{L} . The FDR (7a) is most easily solved for \mathbf{C}_0 in the eigenspace of \mathbf{B} (Penland and Sardeshmukh, 1995), and then transformed back to the spherical harmonic space. \mathbf{C}_τ is then calculated from (7b) using the fact that $\exp(\mathbf{B}\tau) = \mathbf{E}\mathbf{\Lambda}\mathbf{E}^{-1}$, where \mathbf{E} is the matrix with the eigenvectors of \mathbf{B} as columns, λ are the eigenvalues of \mathbf{B} , and $\mathbf{\Lambda}$ is a diagonal matrix with elements $\exp(\lambda_j\tau)$. Finally, the diagonal elements of \mathbf{C}_0 and \mathbf{C}_τ (the variance and lag-covariance maps) are transformed from spectral to grid space for display.

3. Results for the winter mean background flow.

Using the 13 year winter (December - February) mean winds to compute \mathbf{L} , we solve the FDR with the parameter settings given in section 2. Our state variable $\tilde{\mathbf{x}}$ contains the spherical harmonic expansion coefficients for perturbation streamfunction, so C_0 represents streamfunction variance. The assumption $\mathbf{Q} = \epsilon \mathbf{I}$ therefore amounts to the assumption that all the spherical harmonic coefficients of streamfunction are excited equally, and independently, by our stochastic forcing $\tilde{\mathbf{F}}_s$. In general, the solution C_0 of the FDR (7a) will depend upon the norm in which \mathbf{Q} is assumed to be white. Unless noted otherwise, all of the results shown in this paper use $\mathbf{Q} = \epsilon \mathbf{I}$ in the streamfunction norm. Sensitivity of the solution to the choice of norm is discussed further in section 5.

Figs. 1a and 1b show the observed and predicted 400 mb DJF high-frequency streamfunction variance, respectively. The scaling constant ϵ in (7a) has been chosen so that the maximum 400 mb eddy kinetic energy of the solution matches observations (see Fig. 2). It is clear that the simple theory (7) is able to capture the most important features of the observed distribution, the Atlantic and Pacific storm tracks. The main deficiencies appear to be that the simulated Atlantic storm track is too far north, and too little eddy activity penetrates the mean ridge in the eastern Pacific.

The relative contributions to C_0 from barotropic and baroclinic energy interactions with the basic state can be estimated by contrasting Fig. 1b with Fig. 1c, which is the result of a calculation in which only the barotropic part of the observed DJF winds were used to compute \mathbf{L} . Since there are no basic state temperature gradients in the latter calculation, the eddy variance is maintained solely by the stochastic forcing and barotropic energy conversions. The domain integrated streamfunction variance is about 37% of that in Fig. 1b, indicating that baroclinic energy conversions play a dominant role in maintaining eddy variance in our stochastically forced, baroclinically stable model. However, the barotropic calculation still yields localized regions of eddy variance in the Atlantic and Pacific, although the dynamics of eddy growth supporting these

"storm tracks" are clearly different from those in the full baroclinic calculation. When the zonally varying component of the barotropic basic flow is removed, the eddy variance is reduced even further (Fig. 1d), indicating that the barotropic energy source for the eddy variance in Fig. 1c is associated primarily with the zonally varying part of the barotropic deformation field. When only the solid body rotation component of the barotropic zonal wind is retained in the basic state, the domain integral of streamfunction variance (not shown) is reduced to about 27% of the full baroclinic case (Fig. 1b). For this extreme distortion of \mathbf{L} , there are no barotropic or baroclinic sources of energy for the eddies, and the variance is maintained solely by the stochastic forcing. This implies that the about 73% of the total eddy variance in the full baroclinic calculation (Fig. 1b) is associated with energetic interactions with the mean flow, and is not forced *directly* by $\tilde{\mathbf{F}}_s$.

If $\tilde{\mathbf{y}} = \mathbf{M}\tilde{\mathbf{x}}$, then the zero lag covariance matrix of $\tilde{\mathbf{y}}$ is $\mathbf{M}\mathbf{C}_0\mathbf{M}^T$, and its diagonal elements displayed in grid space constitute a variance map of $\tilde{\mathbf{y}}$. Fig. 2 shows the observed and predicted eddy kinetic energy at 400 mb determined in this manner. Again, the Atlantic and Pacific storm tracks, defined now in terms of eddy kinetic energy instead of streamfunction variance, are quite well simulated by the model. Note that both the simulated and the observed Atlantic storm tracks are stronger than their Pacific counterparts, suggesting that at least some of the dynamics associated with the "midwinter suppression" of eddy activity in the Pacific noted by Nakamura (1992) are being captured by the model. We will return to this point in section 4.1.

In addition to producing realistic looking variance maps, our theory (7) can also reproduce the observed heat and momentum fluxes, lag covariances and one-point lag correlation maps quite well, as we will now demonstrate.

3.3 Simulated eddy fluxes of heat and momentum.

Transports of heat and momentum by subweekly time scale eddies play an important role in maintaining the observed time mean flow (Hoskins et al 1983; Lau and Holopainen 1984, Valdes and Hoskins, 1989) as well as large scale, persistent flow anomalies (e. g. Green 1977, Kok and

Opsteegh 1985, Hoskins and Sardeshmukh 1987, Held et al 1989, Nakamura and Wallace 1990). Although nonlinear feedbacks between high-frequency eddies and the low-frequency flow make it difficult to establish causal relationships, it would still be useful to know what changes in the storm tracks (including the attendant fluxes of heat and momentum) could be expected to accompany a change in the quasi-stationary large scale flow. Furthermore, if a method were available to predict such changes, it could be used as a basis for parameterizing the effects of high-frequency eddies in a model of low-frequency atmospheric variability. Most previous efforts in this direction have utilized the fastest growing normal modes of the background flow as a basis for estimating changes in eddy fluxes (Frederiksen 1983, Robertson and Metz 1989; 1990). One exception is the work of Branstator (1995), who used an ensemble of short (5 day) integrations from random initial conditions, using a linearized GCM, to simulate changes in eddy fluxes accompanying low frequency flow anomalies in a long run of the same GCM. Our goal is to construct a model of synoptic eddy fluxes that not only serves as a parameterization, but also forms the basis of a self-consistent theory for those fluxes.

To assess the feedback of the high-frequency eddies on the time mean flow, we use the two-level model equations to determine streamfunction tendencies associated with eddy fluxes of vorticity and temperature. The model's time mean vorticity equation may be written

$$\frac{\partial}{\partial t} \nabla^2 \bar{\psi}_j + J(\bar{\psi}_j, \nabla^2 \bar{\psi}_j + 2\mu) + \nabla \cdot 2\mu \nabla \bar{\chi}_j^{mean} = -\left((2-j)r_M + v \nabla^4\right) \nabla^2 \bar{\psi}_j - \overline{J(\psi'_j, \nabla^2 \psi'_j)} - \nabla \cdot 2\mu \nabla \bar{\chi}_j^{eddy}, \quad (16)$$

where overbars represent a long time mean and primes indicate eddies. The quantities $\bar{\chi}_j^{eddy}$ and $\bar{\chi}_j^{mean}$ are obtained by solving the QG "ω-equation" forced by transient eddy fluxes and mean advections, respectively. The mean streamfunction tendency associated with the synoptic-eddy vorticity fluxes contains a part associated with the second term on the right hand side of (16), as well as a contribution associated with the differences between the synoptic-eddy vorticity fluxes at 400 and 800 mb, which enters through $\bar{\chi}_j^{eddy}$. These two components can be thought of as the barotropic and baroclinic components of the vorticity flux forcing, respectively. The contribution to

the mean streamfunction tendency associated with transient eddy heat fluxes only enters through $\overline{\chi_j^{eddy}}$.

Fig. 3 shows the streamfunction tendency associated with synoptic-eddy vorticity fluxes, obtained in this manner, from both observations and from the solution of the FDR (7a). As before, the free parameter ε is chosen so that the maximum 400 mb eddy kinetic energy produced by the FDR matches observations. The model captures the general tendency for storm track eddy fluxes of momentum to accelerate the Pacific and Atlantic jets, although the values are about twice as large as observed.

The simulated streamfunction tendency associated with synoptic-eddy heat fluxes matches observations very well in both position and magnitude (Fig. 4). The only deficiency is the tendency for the simulated heat fluxes to be too strong in the Atlantic storm track. Our model appears to correct the problem noted by both Branstator (1995) and Frederiksen (1983), that is, when the eddy amplitudes are scaled so that the simulated momentum fluxes match observations, the heat fluxes are much too large. In fact, our theory appears to have the opposite problem, i.e. the simulated momentum fluxes are too large when the heat fluxes match observations. At this time we do not have an explanation for this behavior.

3.4. Lag covariances and propagation characteristics.

NSP examined whether the FDR for a barotropic model linearized about the observed 200 mb flow could account for the observed statistics of low-frequency flow anomalies in the atmosphere. They found that although the model could be tuned to produce fairly realistic simultaneous covariances, the corresponding lag-covariances did not match observations very well. Here we examine whether a baroclinic stochastic model with forcing that is white in both space and time (in the streamfunction norm) can produce lag-covariances and one point lag correlation maps similar to those observed. This is a fairly demanding test, since we are essentially asking the model to

reproduce the observed frequency power spectra and propagation characteristics of high-frequency transients.

Figure 5 shows the 1.5 day lag streamfunction covariance computed from observed high frequency transients and the FDR (7). Both the observed and simulated lag covariances are predominately negative, with patterns similar to the simultaneous covariances but with less amplitude. The simulated lag covariance is somewhat weaker (stronger) than observed in the Pacific (Atlantic) storm track. Results for other lags produce similar agreement between model and observations. Since the observations are subjected to a eight day highpass filter, the lag covariance falls of to zero at about five days. The five day lag covariance computed from the model solution, is small but nonzero, indicating that some low-frequency motions are excited by the white noise forcing. The contribution of these low-frequency motions to the eddy statistics shown here is negligible.

One-point lag-correlation maps are often used to illustrate the statistical structure and evolution of high-frequency disturbances (see e. g. Wallace et al 1988). Figure 6 shows one-point lag-correlation maps of both observed and simulated 400 mb streamfunction for lags -2, 0 and +2 days for a base point near the entrance of the Pacific storm track. The one-point lag-correlation maps for the simulated high-frequency transients are a particular row (column) of C_τ for negative (positive) τ , transformed to grid space, and normalized by the corresponding diagonal element of C_0 . There is a good correspondence between the observed and simulated correlation maps, indicating that the structure and propagation characteristics of the high-frequency transients are well simulated in the Pacific storm track. The downstream energy propagation of eddy energy in the Pacific jet is slightly faster than observed, which may account for the fact that the simulated lag covariances are too weak (Fig. 5). Also, the horizontal tilts of the simulated eddies in the Pacific jet are too strong, consistent with the unrealistically large simulated momentum fluxes noted in the previous section.

The lag-correlation maps for a base point at the beginning of the Atlantic storm track are shown in Fig. 7. Here discrepancies between simulated and observed eddies are more apparent.

particularly for the +2 day correlations. The zonal scale of the simulated eddies is somewhat too short, the +2 day correlation is too large, and the eddies tend to propagate too far north and east, compared to the observed eddies.

3.5. Eddy growth characteristics.

Since there is no exponential instability in our model, the simulated storm track eddies must either be directly forced by the stochastic forcing, or grow through transient energetic interactions with the mean flow. Some indication of the relative roles of these processes is given in Fig. 1 and the accompanying discussion. Here we examine this issue in greater detail.

Since the simulated eddy variance is much larger when barotropic and baroclinic energy sources are included in the basic state (Fig. 1), and the solution variance is spatially localized while the forcing is not, energetic interactions with the mean state are clearly important. The maximum amplification (MA) curve (Penland and Sardeshmukh 1995, Borges and Sardeshmukh 1995) is a succinct way of summarizing the behavior of linear perturbations to a given mean flow. It quantifies the maximum growth possible over a given time interval in the absence of forcing. Figure 8 shows the MA curve for the 13 winter mean flow, i.e. the maximum singular values of $\mathbf{G}(\tau)$ as a function of τ , together with the linear evolution of selected optimal linear perturbations, whose initial structure is given by the corresponding right singular of \mathbf{G} . Peak amplifications are about twelvefold and are achieved at about 3.5 days. The evolving perturbations have essentially reached normal mode form by 15 days. As in the barotropic case analyzed by Borges and Sardeshmukh (1995), perturbations optimized for short time intervals are highly suboptimal for longer time intervals. However, as highlighted in Fig. 1, in our model perturbations grow primarily through baroclinic energy conversions, although barotropic energy conversions do contribute, particularly for short optimization intervals.

The MA curve merely reveals the possibility of growth over a given time interval. Whether this growth is actually achieved in the stochastically forced system (6) depends upon whether the

state vector has a significant projection onto the subspace of growing optimal perturbations at any given time (Sardeshmukh et al, 1996), and whether the white noise forcing interferes strongly with the free evolution of those growing perturbations. If one considers the free linear evolution of an initial distribution of perturbations that is random, i. e. the covariance matrix of the initial perturbations is \mathbf{I} , then the expected ratio of the ensemble mean variance at any time τ to the initial variance is given by $\text{Tr}(\mathbf{G}\mathbf{G}^T)$, where, as before, $\mathbf{G} = \exp(\mathbf{B}\tau)$ is the linear propagator matrix. By definition, the quantity $\text{Tr}(\mathbf{G}\mathbf{G}^T)$ is simply the sum of the squared singular values of \mathbf{G} . In contrast, the maximum amplification factor plotted in Fig. 8 is just the square of the largest singular value. If the covariance matrix of the initial perturbations is given by \mathbf{C}_0 , then the expected ensemble mean variance at time τ is $\text{Tr}(\mathbf{G}\mathbf{C}_0\mathbf{G}^T)$.

In Fig. 9 we have plotted both the ensemble mean streamfunction variance for free linear integrations of length τ from random initial conditions and initial conditions whose covariance structure is identical to that obtained from solution of the FDR. Both curves have been normalized by the streamfunction variance of the initial perturbations. The ensemble mean streamfunction variance of the free linear integrations from random initial conditions falls off to about one half its initial value in one day, indicating that although rapid growth is possible, it is not probable with such an initial distribution. Starting from initial conditions corresponding to solutions of the stochastic model (4), the ensemble mean streamfunction variance decays somewhat more slowly, reaching half its initial value around day 1.75. Penland (1989) shows that the global error incurred by neglecting the white noise forcing in the initial value problem is $\text{Tr}(\mathbf{C}_0 - \mathbf{G}\mathbf{C}_0\mathbf{G}^T)$, where \mathbf{C}_0 is the modeled covariance matrix (found from the FDR, including stochastic forcing). The total error variance associated with neglecting the stochastic forcing term is also shown in Fig. 9. Clearly, the effect of the stochastic forcing rapidly becomes important, violating the assumption of free linear evolution after one or two days. In other words, if one were to take realizations of our stochastically forced model and make predictions by evolving those realizations freely using the linear dynamical operator of the model, skill would significantly degraded by day 2 and all skill would be lost by about 4 days. This does not mean that stochastic forcing dominates the budget

equation for eddy energy, or that energetic interactions with the mean flow are unimportant. In fact the opposite conclusion would be reached from such a budget calculation. However, the stochastic forcing does disrupt the eddy structures significantly, so that the evolution of perturbations cannot be described by the linear dynamical operator \mathbf{G} alone beyond 4 days.

We have also examined whether forecasts made by evolving *observed* patterns of high-frequency streamfunction at 400 and 800 mb using the linear propagator matrix (\mathbf{G}) of our model have any useful skill. Here we use pattern correlations as a measure of skill. For the stochastic model, using observed high-frequency data as initial conditions, it can be shown that the expected pattern correlation as a function of forecast lead time is

$$r = (1 - \frac{\text{Tr}(\mathbf{C}_0 - \mathbf{G}\mathbf{C}_0\mathbf{G}^T)}{\text{Tr}(\mathbf{C}_0)})^{1/2}, \quad (17)$$

where \mathbf{C}_0 is the covariance matrix of observed high-frequency streamfunction. To derive this expression, one must make use of the fact that, for the stochastic model, the forecasts and the forecast errors are uncorrelated. Fig. 10 shows r as a function of forecast lead time for the stochastic model, along with $r_{per} = \text{Tr}(\mathbf{G}\mathbf{C}_0)/\text{Tr}(\mathbf{C}_0)$ (the expected pattern correlation for a persistence forecast) and r_{MRF} (the pattern correlation for the current T126 global spectral model used for medium-range forecasting at NCEP). To compute r_{MRF} we use 88 forecasts of 250 mb high-frequency streamfunction verifying during DJF 1995/96. The MRF forecast dataset at our disposal contains forecasts sampled twice daily out to seven days. Since the time series for each forecast contains only 15 points, we were forced to use a much simpler and more compact high-pass filter; deviations from running ten point means. Given that (1) this high pass filter is different from what was used to construct \mathbf{C}_0 in (17), (2) we are using a different pressure level (250 mb instead of 400 and 800 mb), and (3) only 88 forecasts from one winter are used, the comparison between the two models can be interpreted in very general terms. Fig 10 shows that the stochastic storm track model outperforms persistence by a wide margin at all forecast ranges, and appears to have skill comparable to operational forecast models for forecast ranges of less than three days. This suggests that complex nonlinearities and physical processes represented in

operational forecast models may do not contribute very much to the *general* skill of *short-range* forecasts of high-frequency, synoptic scale weather systems. However, given the caveats just mentioned, a more precise comparison is clearly warranted.

4. Simulation of annual and interannual variations of the storm tracks.

In the previous section we established that the stochastic model is capable of simulating many important features of the observed climatological storm tracks, including the geographical distribution of variance, lag covariance, and fluxes of heat and momentum. To be useful as a parameterization of the effects of synoptic eddies, the model must also be able to predict what changes in these eddies are associated with specified low-frequency changes in the background flow. To test the utility of our model in this regard, we have examined the sensitivity of the simulated storm tracks to mean flow changes associated with the observed annual cycle, as well as observed interannual variability.

4.1 Modeling the annual cycle of the storm tracks.

Nakamura (1992) examined the annual evolution of the Northern Hemisphere storm tracks during the six month cold season (October through April). He found that although the Pacific is strongest in January, the Pacific storm track actually is weaker in January than in November and April. Thus, the Pacific storm track is weaker than the Atlantic storm track in January, even though the Pacific jet itself is consistently stronger than the Atlantic jet. In addition, the relative amplitudes of the Pacific and Atlantic storm tracks in mid-winter is opposite to what one would expect from simple indices of baroclinic growth potential (which are typically linearly related to the vertical shear of the basic flow). To see if our model can reproduce these aspect of the seasonal cycle, we have solved the FDR using January and April mean states. The parameter ϵ is set so that the maximum eddy kinetic energy at 400 mb matches observations in each case.

Fig. 11 shows the observed and simulated eddy kinetic energies for both cases. The model appears able to capture some important aspects of the seasonal cycle of the storm tracks. As observed, the simulated Pacific storm track is weaker than the Atlantic storm track in January, and stronger than the Atlantic storm track in April. However, if equal forcing amplitudes (i.e identical ϵ) were used in both cases, the model would not produce a Pacific storm track that is weaker in January than April. Thus, the model does not capture the mid-winter minimum in the Pacific storm track, but it *is* able to simulate changes in the relative amplitudes of the Pacific and Atlantic storm tracks during the seasonal cycle. The model also captures the observed tendency for the downstream end of the Atlantic storm track and the upstream end of the Pacific storm track to be more connected in April than January, associated with enhanced propagation of eddy activity over Northern Europe and Asia.

4.2. Modeling storm track shifts associated with interannual variability in observed stationary waves.

Extratropical stationary wave anomalies often associated with El-Nino/Southern Oscillation (ENSO) are known to be associated with significant changes in the storm tracks (Lau 1988). In addition, anomalous eddy transports of heat and momentum associated with these storm track shifts are a important factor in maintaining those stationary wave anomalies (Kok and Opsteegh 1985, Held et al 1989, Hoerling and Ting 1994). In this section we examine whether the stochastic model can reproduce the storm track shifts associated with stationary wave anomalies observed during the 13 winters period beginning December 1985.

It is important to recall from the discussion in section 1 that the averaging period used here (90 days) may be too short to insure that all (or even most) of the observed storm track anomalies are directly linked to stationary wave anomalies. For instance, one or two extreme cases of cyclogenesis may significantly affect the 90 day mean high frequency eddy kinetic energy, but may be considered random events not linked to the large scale flow pattern in a statistically significant

way. Conversely, a single large-scale flow anomaly, such as a block, that persists for only one or two weeks (or two or three synoptic eddy lifetimes) may significantly affect the seasonal mean flow, but may not necessarily have a corresponding impact on the seasonally averaged high-frequency eddy statistics. Therefore, the stochastic model should not be expected to reproduce the observed storm track anomalies exactly. In fact, if the stochastic model were "perfect", in the sense that it could exactly reproduce the observed long-term statistics of high-frequency eddies, one would expect it to extract only the predictable, or statistically significant, signal associated with a given stationary wave anomaly.

We have solved the FDR (7a) for each of the 13 observed DJF mean basic states, but now using a flow-dependent linear damping in \mathbf{D} in (4) which reduces the growth rate of the most unstable eigenmode for each winter to $-1/20 \text{ days}^{-1}$. The reason for this choice of damping will be discussed in detail in section 5b. Briefly, the growth rate for the most unstable eigenmode for each DJF mean basic state ranges from 0.0394 days^{-1} (for DJF 1985/86) to 0.0966 days^{-1} (for DJF 1993/94). It was found that the $\text{Tr}C_0$ is quite sensitive to the extra damping included in \mathbf{D} only when that damping is very close to the e-folding time of the most unstable mode (see Fig. 16). Therefore, using a fixed \mathbf{D} of $1/10 \text{ days}^{-1}$ for all cases resulted in a very large amplitude storm tracks for the DJF 1993/94 basic state (for which the e-folding time of the most unstable mode is close to 10 days). We chose a flow dependent \mathbf{D} to avoid this nearly resonant behavior. We could have circumvented this by repeating all the calculations with a stronger α , say $\alpha = 1/5 \text{ days}^{-1}$, but then we would have had to justify such a strong value.

Even if sampling considerations prevent us from using the storm track model to simulate storm track anomalies for individual seasons, one should expect the model to be able to simulate the *statistics* of the interannual variability of the storm tracks. Fig. 12 shows the observed and simulated standard deviation of the 13 400 mb high-frequency streamfunction variance maps for the 13 winters. The largest interannual variability is near the downstream end of the storm tracks in both models and observations, although the simulated interannual variability is somewhat stronger than observed in the Pacific basin. This suggests that, on average, the model possesses

some skill in simulating the sensitivity of the storm tracks to observed interannual stationary wave variability. We find this quite encouraging, given the extreme simplicity of the model.

The results of the 13 calculations are summarized in Table 1. Anomalies of high-frequency streamfunction variance for the observations (simulations) are computed relative to the observed (simulated) 13 winter mean. Both the observed and simulated variance anomalies are smoothed to T12 resolution, since the unsmoothed observed fields were quite noisy. The average of the 13 simulated variance maps is nearly identical to that computed from the 13 winter mean basic state (Fig. 1b). The average anomaly correlation for the 13 pairs of simulated and observed anomaly variance maps is 0.3, indicating that perhaps 1) there are significant systematic errors in the storm track model, and/or 2) a large fraction of the anomalous high frequency eddy variance on seasonal time scales is not directly linked to the seasonal mean anomalous stationary wave pattern. Determining the relative importance of these two explanations is difficult with observations, but a large ensemble of general circulation model (GCM) simulations with fixed boundary conditions but different initial conditions could be used to address this question. The ensemble mean storm tracks would then be unambiguously related to the ensemble mean anomalous stationary wave pattern for a given 90 day period, if the sample size were large enough. This is a topic of ongoing research.

Fig. 13 shows the observed and simulated anomalous storm tracks for three cases, one with the best anomaly correlation (top), one with the worst (middle), and an ENSO case (bottom). In the best case (DJF 1994/95), the model appears able to capture virtually every detail of the observed storm track anomalies. Conversely, in the worst case (DJF 1984/85) the model clearly has no skill. The ability of the model to correctly simulate the storm track anomalies in some winters and not others could be related to regime-dependent systematic errors in the model, or could be due to simply to chance. For example, in the hypothetical GCM ensemble integration mentioned above, in some cases one individual member of the ensemble could be very close to the ensemble mean, so that the statistically significant signal would appear to be manifested in one realization. Another possibility is that there is something about the DJF mean flow for 1994/95

that "locks" in the storm tracks, so that they are very strongly constrained by the anomalous stationary waves.

The DJF 1982/83 case has been included since observed stationary wave anomalies during this extreme ENSO event have been well documented (see e. g. Hoerling and Ting 1994, Fig. 4a). The dominant features of the observed storm track anomalies are the southward shift and eastward extension of the Pacific storm track, and the northward shift in the Atlantic storm track. These shifts are consistent with the observed southward and eastward extension of the Pacific jet and the northward shift of the Atlantic jet. The latter feature is associated with the particular phase of the North Atlantic Oscillation (NAO) that was persistent during that winter, and is unlikely to be directly related to ENSO. The stochastic model is able to capture the observed northward shift of the Atlantic storm track quite well. In the Pacific basin, the model does produce an eastward shift of the Pacific storm track, although the region of negative anomalous streamfunction variance in the Gulf of Alaska is weaker than observed. Qualitatively, the model appears able to capture the dominant storm track signal associated with ENSO, at least in some cases.

5. Sensitivity.

5.1 Sensitivity to the choice of norm.

As was mentioned in section 2, even if one specifies the stochastic forcing to be incoherent in space, one has to specify in what space it is so. In general, the solution of (7a) is will depend upon the norm in which it is solved. To explore this dependence, we have solved the FDR for the 13 winter mean DJF basic state in three norms, streamfunction, kinetic energy and vorticity. The scaling constant ϵ is chosen so that the maximum eddy kinetic energy matches observations in each case. The state variable in the kinetic energy norm is $\sqrt{n(n+1)/4} \hat{\psi}_j$, where $\hat{\psi}_j$ are the spherical harmonic coefficients of ψ'_j and n is the total wavenumber. With this choice of state variable, the trace of the covariance matrix is the volume integrated perturbation kinetic energy,

$$\frac{1}{2} \sum_{j=1}^2 \int_{-1}^{+1} \int_0^{2\pi} \frac{1}{2} \nabla \psi_j \cdot \nabla \psi_j d\lambda d\mu.$$

The 400 mb eddy kinetic energy maps calculated by assuming $\mathbf{Q} = \mathbf{EI}$ in the kinetic energy and vorticity norms are shown in Fig. 14. The solution in the streamfunction norm was shown in Fig. 2b. The gross features of the solution in the vorticity norm are similar to the other two norms, but there are significant differences. These differences appear larger when comparing streamfunction variance. These differences arise mainly because, relative to the streamfunction norm, solution of the FDR with $\mathbf{Q} = \mathbf{EI}$ in the vorticity norm forces the larger scales (small n) much more strongly. Thus, the solution to the stochastically forced problem is dominated by planetary-scale, low-frequency disturbances. On the other hand, as is clear from comparing Fig. 2b with Fig. 14a, we see that the solutions are nearly identical in the kinetic energy and streamfunction norms. In fact, the solution of the FDR appears to be remarkably insensitive to the norm chosen, as long as the largest spatial scales are not forced too strongly relative the synoptic scales of interest here.

One can also infer \mathbf{Q} given an observed \mathbf{C}_0 , this has been referred to as a "backward" application of the FDR (NSP). The \mathbf{Q} thus computed is guaranteed to be symmetric, but not positive definite, so it may need to be truncated to retain only the positive definite part (Penland and Matrosova 1994). We have computed a truncated positive definite \mathbf{Q} using observed covariances of high-pass filtered streamfunction at 400 and 800 mb. Fig. 15a shows the diagonal elements of this \mathbf{Q} , displayed in grid space. There is some geographical coherence to the forcing, particularly over North America. However, if we use this forcing to solve the forward FDR the \mathbf{C}_0 produced (Fig. 15b) is not that much different than the solution computed with $\mathbf{Q} = \mathbf{EI}$ in the streamfunction norm (Fig. 1b)². The Atlantic storm track is somewhat stronger than the Pacific storm track, in accordance with observations, when the geographically coherent \mathbf{Q} is used. This is consistent with the region of concentrated forcing over North America, just upstream of the Atlantic storm track (Fig. 15a). Overall, we find it remarkable that the simple model (4) is able to produce such

²The \mathbf{C}_0 computed using the \mathbf{Q} from the backward FDR is not identical to the observed \mathbf{C}_0 , because of the truncation that was necessary to make \mathbf{Q} positive definite.

realistic storm tracks when no observations are used in the specification of \mathbf{Q} , other than the single amplitude scale factor ϵ .

5.2 Sensitivity to \mathbf{D} .

The damping operator $\mathbf{D} = -\alpha \mathbf{I}$ must be large enough to insure that \mathbf{B} is stable. In the limit $\alpha \rightarrow \infty$, \mathbf{B} is a diagonal matrix with diagonal elements $-\alpha$, so that the FDR then yields $\mathbf{C}_0 = \mathbf{I} / 2\alpha$ (NSP). Conversely, when $\alpha \rightarrow -\lambda_r^{\max}$, where λ_r^{\max} is the growth rate of the least damped mode of \mathbf{B} , the resulting eddy statistics tend to be dominated by a structure nearly identical to that of the least damped mode of \mathbf{B} . This can be understood by noting that the solving the FDR (7) for \mathbf{C}_0 yields

$$\mathbf{H}_{ij} = -\frac{\left[\epsilon \mathbf{E}^{-1} (\mathbf{E}^{-1})^T \right]_{ij}}{\lambda_i + \lambda_j^*} \text{ and } \mathbf{C}_0 = \mathbf{E} \mathbf{H} \mathbf{E}^T, \quad (18)$$

where \mathbf{E} is the matrix with the eigenvectors of \mathbf{B} (or \mathbf{L} , since the addition of a linear damping does not change the eigenvectors) as columns, and λ are the eigenvalues of \mathbf{B} (Penland and Sardeshmukh 1995). If \mathbf{B} were normal, the eigenvector matrix \mathbf{E} would be orthogonal, and the trace of the covariance matrix would be inversely proportional to the (real) eigenvalues. Therefore, the variance would be dominated by the least damped mode. Since \mathbf{B} is nonnormal in this case, this variance need not be dominated by the least damped mode, but in practice, when the damping parameter α is such that \mathbf{B} is near resonance, the least damped mode does indeed dominate (i. e. the leading EOF of \mathbf{C}_0 explains nearly all of the variance, and its structure is nearly identical to the least damped mode of \mathbf{B}).

Fig. 16 summarizes the sensitivity of the solution to the damping parameter α . As expected from equation (12), when the most unstable mode is only weakly damped ($\alpha \rightarrow -\lambda_r^{\max}$), the variance of the solution (as measured by $\text{Tr} \mathbf{C}_0$) is very large. In this limit, the leading two EOFs

of C_0 , which combine to represent a single oscillatory structure almost identical to that of the least damped eigenmode, explain a very large fraction of the total variance. As the time scale for decay of the least damped mode is decreased, the fraction of variance explained by the leading EOF is reduced, so that for damping rates less than 15 days, the leading EOF explains less than ten percent of the variance. Therefore, unless α is defined such that the least damped mode of \mathbf{B} is nearly neutral, the least damped mode has no special significance.

Maps of the diagonal elements of C_0 , displayed in grid space, show some sensitivity to the value of α chosen. For small α , the maps essentially show the amplitude pattern of the least damped mode, which happens to be somewhat higher in the Atlantic storm track, relative to the Pacific storm track. Since the structure of the most unstable (or least damped) mode can be quite sensitive to small variations in model parameters, basic state and resolution (see e. g. Borges and Sardeshmukh 1995) it seems sensible to choose an α large enough so that no single structure dominates the solution. For α between $1/20 \text{ days}^{-1}$ and $1/5 \text{ days}^{-1}$ the gross characteristics of the solution are quite similar. However, there is a tendency for the variance to become more localized in the region of strongest temperature gradients as α is increased. Qualitatively, this means that the simulated Pacific storm track becomes stronger relative to the Atlantic storm track as α is increased. When the damping is strong, the solution essentially becomes a local balance between stochastic forcing and dissipation, with very little propagation away from the source regions. We have chosen a value of $\alpha = 1/10 \text{ days}^{-1}$ (corresponding to a decay time scale of 18 days for the least damped mode) between the two extremes

6. Discussion and conclusions.

In this paper we have attempted to explain the observed structure of the Northern hemisphere wintertime synoptic-scale variability, given the structure of the planetary scale background flow. We have used an extremely simple dynamical model for this purpose. We conjecture that synoptic eddy evolution, *on average*, can be viewed as stochastically forced

disturbances evolving on a baroclinically *stable* background flow, so that the eddy statistics are identical to those of the multivariate first-order linear Markov process (4). We then use well known results from the extensively developed theory of Markov processes to determine those statistics through (7).

To keep the theory simple and as free as possible of arbitrary adjustable parameters, the deterministic part \mathbf{B} of the Markov process is specified to be a linearized two-level quasi-geostrophic model \mathbf{L} of extratropical synoptic eddies plus a uniform damping $\mathbf{D} = -\alpha \mathbf{I}$. The two-level QG model was chosen because it is the simplest model incorporating the basic baroclinic dynamics of extratropical synoptic eddy development; and the uniform damping \mathbf{D} because it represents the simplest possible accounting of nonlinear saturation effects. The stochastic forcing part of the Markov model is kept simple by specifying it as geographically incoherent white noise with covariance $\mathbf{Q} = \varepsilon \mathbf{I}$. Our Markov model (4) is thus completely defined by the nondivergent part of the background flow at two levels (400 and 800 mb), three 'standard' model damping parameters (representing low-level Rayleigh damping, mid-tropospheric thermal damping, and biharmonic diffusion), one static stability parameter, plus α and ε . The value of α actually specified in most of the calculations ($1/10 \text{ days}^{-1}$) is small enough to be within the range of uncertainty of the 'standard' model damping parameters, so α need not necessarily be viewed as an additional parameter. Although we did not explore this, we could conceivably have obtained similar results by setting α to zero and making minor adjustments to the other damping parameters. In that case, \mathbf{B} would have been identical to \mathbf{L} , and the only extra parameter needed to define our Markov model would have been ε . This parameter is essentially a scaling constant, chosen to match observed amplitudes with simulated amplitudes given by a linear theory. It has have no effect on the predicted patterns.

It is important to recognize that (4) is only one out of an infinite number of first-order linear Markov models applicable to this problem. In particular, we did not determine the dynamical operator \mathbf{B} empirically, as done for example by Penland and Sardeshmukh (1995) and DelSole (1996). These authors determined \mathbf{B} as the solution of (6) with specified observed (or model

generated) covariances C_0 and C_τ . We also did not determine \mathbf{D} (and therefore \mathbf{B}) by actually regressing observed nonlinear and forcing terms against $\tilde{\mathbf{x}}$ in (3). It is possible that \mathbf{B} obtained through either of these approaches could give better results than shown here. However, for an N -dimensional Markov process, we would then have N^2 model parameters contained in \mathbf{B} , instead of the $2 + 4 + N$ (needed to describe the background flow) of our model, and so the "explaining power" of such an empirical model would be correspondingly smaller. Another very important reason for choosing $\mathbf{B} = \mathbf{L} - \alpha \mathbf{I}$ is that the eigenstructures of \mathbf{B} and \mathbf{L} are the same, and so the deterministic dynamics \mathbf{B} of our model are the well understood quasi-geostrophic dynamics of synoptic eddies. The only difference is that the eddies are now damped.

Despite these drastic simplifications, our model performs remarkably well. It simulates all the major features of the wintertime climatological storm tracks, such as the geographical distributions and intensities of the eddy variances, lagged covariances, kinetic energy, and vorticity and heat fluxes (Figs 1-5). Furthermore, it simulates not only the aggregate statistical structure of the eddies as revealed by these measures, but also the statistical structure of the eddies themselves in the Pacific and Atlantic storm tracks (Figs 6-7). Indeed, (4) used as a forecast model for the individual observed eddies easily outperformed a persistence forecast model, and had comparable skill to that of the operational NCEP forecast model for forecast ranges of up to 2 days (Fig 10). The model is also able to simulate correctly the change in the relative strengths of the Pacific and Atlantic storm tracks from January to April (Fig 11), and is able to capture much of the interannual variability of the wintertime storm tracks (Fig 12). We stress again that it is able to do all this given only the planetary scale background flow plus a few damping and scaling parameters. The results are rather insensitive to the precise values of these parameters, so long as α was not such that the least damped mode of \mathbf{B} is almost neutral (Fig 16). The results are also rather insensitive to the specification of the space in which the stochastic forcing was assumed to be white, so long as it did not excite the largest planetary scales of the flow much more strongly than other scales.

Even a cursory comparison of Figs 1a and 1b immediately suggests the power of this simple theory. The idea that synoptic eddies behave on average as stochastically forced eddies

evolving on a baroclinically stable background flow clearly goes a long way towards explaining the general structure of observed storm tracks. In our theory the eddies are being forced uniformly everywhere on the hemisphere, on all scales; the reason they grow near the Pacific and Atlantic jets into recognizable weather systems is that they can efficiently draw upon the potential (and to a lesser extent, the kinetic) energy available in those jets (Fig 8). *No exponential instability need be invoked.* This is entirely consistent with the view of Farrell (1989). The energy balance in our model is between the stochastic forcing and baroclinic and barotropic energy extraction from the sheared flow on the one hand, and eddy dissipation on the other. As suggested by Fig 1, of the three energy sources available to the eddies, they draw most heavily upon the available potential energy source. The stochastic source is of secondary importance.

It is interesting to contrast our results with those of DelSole (1996). Using a Markov model, he attempted to model the synoptic eddy variability simulated in a two-layer nonlinear quasi-geostrophic channel model, with zonally symmetric forcing and boundary conditions, with mixed results. Given that he was only attempting to explain the variability of a 2-layer model, and not of the observed atmosphere as we have done, his aim was less ambitious, and therefore his relative lack of success is all the more puzzling. One possible explanation is that we considered a zonally varying background state, and he did not. Eddies growing in our model can leave the baroclinically active regions and decay by barotropic processes, as shown in Figs 6 and 7. In DelSole's model, eddies grow on a zonally symmetric basic state and are confined to a re-entrant channel, and hence never enter a region unfavorable for eddy growth. Nonlinear processes may then be considerably more important in halting the growth of eddies in his model. Another difference is that DelSole was trying to explain variability on all timescales in his model, not just high-frequency synoptic-scale variability. It is noteworthy that NSP tried, but failed, to explain observed low-frequency variability in a stochastically forced linear barotropic model using methods similar to that described here. This indicates that one fundamental difference between observed low and high frequency variability is that the details of the forcing are very important in explaining the former, while energetic interaction with the background flow is the dominant process

controlling the dynamics of the latter. In other words, the relative importance of processes incorporated in \mathbf{B} versus \mathbf{Q} is opposite for the two types of variability.

It is also interesting to contrast our analysis with that of Branstator (1995). He sought to explain the storm tracks simulated in a model - this time a multi-level GCM run in perpetual January conditions - with a linear storm track model. His results are just as striking as ours, in many respects. His \mathbf{L} operator, in the terminology of our equation (1), is the GCM linearized about its long-term mean state, and his prescription for \mathbf{C}_0 , given this \mathbf{L} , is simply $\mathbf{C}_0 = \varepsilon_b \exp(\mathbf{L}\tau_b)\exp(\mathbf{L}^T\tau_b)$, where τ_b is a time-truncation parameter and ε_b , like our ε , is a scaling constant. This is essentially the (non-stationary) covariance of $\tilde{\mathbf{x}}$ that one would obtain at time $t = \tau_b$ from an ensemble of integrations performed with (1), without the nonlinear and forcing terms, with initial covariance $\varepsilon_b \mathbf{I}$. Indeed this is how Branstator actually determines \mathbf{C}_0 . Note that he did not have a prescription for the lag covariances \mathbf{C}_τ , and therefore no prescription for the eddy power spectra.

Branstator's prescription for \mathbf{C}_0 given \mathbf{L} is thus different from ours (eq. (7)). However, even though it worked just as well in many respects, his prescription does not, in our view, amount to a complete and self-consistent theory of the eddy statistics. The basic difficulty is that his model is not statistically stationary, since he fixes on the evolving covariance at an arbitrary time $t = \tau_b$. As is shown in the paper, the eddy statistics are sensitive to the choice of τ_b . The damping parameter α can be considered to be the analogous free parameter in our model, but it plays a much less important role. As shown in Fig 16, our results were insensitive to its precise value so long as it was not such as to render \mathbf{B} very nearly neutral. One might also question Branstator's specification of the 'initial' covariance being white in a certain norm. Our specification of \mathbf{Q} as white in the streamfunction norm is also somewhat arbitrary, but we show in Figs 14-15 that our results are not crucially dependent upon this choice, as long as \mathbf{Q} does not preferentially excite the largest scales in the model. We suspect the same holds true for the specification of the norm in Branstator's model.

Our model has some notable deficiencies. It does not simulate the northeastward extension of the wintertime Pacific storm track into North America (Fig. 1). In general it produces too strongly tilted eddies in the Pacific and Atlantic storm tracks (Figs 6-7), and thus too strong vorticity fluxes (Fig 3). It also does not capture the mid-winter minimum of the Pacific storm track. And finally, although it is able to simulate the anomalous storm tracks of some individual winters (such as DJF 1994/95; see Fig 13), its general skill was poor in this regard (Table 1).

Some of these failures, especially the poor simulation of the eastern edge of both the climatological Pacific storm track (Fig 1) and its interannual variability (Fig 13), can perhaps be attributed to the simplicity of the two-level quasi-geostrophic \mathbf{L} operator. The inability of the model to capture the Pacific mid-winter minimum may also reflect inadequacies of \mathbf{L} . It would certainly be worthwhile to repeat these calculations with a multi-level primitive-equation model to see if these deficiencies were remedied.

Our model, however, does not consist just of \mathbf{L} , but also \mathbf{D} and \mathbf{Q} , and low-frequency variations of the storm tracks may also be associated with low-frequency variability of \mathbf{D} and \mathbf{Q} . We have stressed that their detailed specification is secondary, and they may in fact be characterized by two single numbers, α and ε . Allowing more complicated prescriptions for \mathbf{D} and \mathbf{Q} could potentially lead to better simulations of annual and interannual variability of the storm tracks, however, lacking any theoretical guidance in this direction, we prefer to leave \mathbf{D} and \mathbf{Q} as simple as possible. In section 4.2, we allowed α to be flow dependent in an attempt to simulate interannual variability of the storm tracks. This was done to avoid the resonant behavior of the FDR when \mathbf{B} is almost exactly neutral. We could have circumvented this problem by choosing a larger α , say $1/5 \text{ days}^{-1}$, but then we would have to justify such a large value. Instead, we chose α such that the least damped mode of \mathbf{B} always decayed with a time scale of 20 days. Even so, α was always small (at most $1/7 \text{ days}^{-1}$) and within the range of uncertainty of the other model damping parameters. More importantly, the simulated interannual variations of the storm tracks (Figs. 12 and 13) is clearly associated mainly with variations in \mathbf{L} , not \mathbf{D} or \mathbf{Q} .

It is remarkable that the model (7) can capture so much of the interannual variability of the storm tracks by invoking only the interannual changes of \mathbf{B} but not of \mathbf{Q} , i.e. by assuming that the symmetric part of \mathbf{BC}_0 remains the same from year to year. This suggests an adjustment between the mean flow (represented by \mathbf{B}) and the synoptic eddy statistics (represented by \mathbf{C}_0) on interannual time scales, which could be viewed as perhaps the broadest possible manifestation of an 'index cycle' in the atmosphere. Nevertheless, the simulation in Fig 13 is clearly far from perfect, and the poor correlations in Table 1 further drive home the point that there is more to the interannual variability of storm tracks than a simple generalized index cycle. Perhaps the variations of \mathbf{Q} , which certainly exist, cannot be ignored at all, even in the simplest theory. As suggested by Fig 11, specifying some variation of \mathbf{Q} would help us simulate the Pacific mid-winter minimum better. We have not pursued such variations further here because we do not have any dynamical theory of them.

Notwithstanding the caveats concerning the simplicity of our \mathbf{B} operator and the simplicity and constancy of our \mathbf{Q} operator, we believe, for reasons discussed in section 1, that the failure of our model to simulate the anomalous storm tracks for individual winters points to a more fundamental problem: that a significant part of the interannual variability of seasonal-mean storm tracks is not parameterizable in terms of seasonal-mean flow anomalies. To that extent, we believe that repeating our calculations with a bigger and better \mathbf{L} operators could lead to diminishing returns, given the reasonably good results already reported here.

In summary, we have presented a simple theory of extratropical storm tracks in which the storm tracks are shown to arise from stochastically forced disturbances reaching relatively large amplitudes in certain preferred regions of the atmosphere through *stable* energy interactions with the local background flow. The theory successfully explains many observed aspects of the climatological wintertime Pacific and Atlantic storm tracks. It is also successful in explaining some aspects of their annual cycle and interannual variability. It can sometimes also predict the anomalous storm tracks during individual seasons; its general ability is however poor in this regard. This failure could be viewed as exposing the inadequacies of the theory. Alternatively, it

could be viewed as highlighting the existence of a portion of the seasonal-mean storm track variability that is unrelated to that of the seasonal-mean flow, and therefore unparameterizable in terms of the seasonal-mean flow.

Acknowledgments

Support for this research was provided through the NOAA Office of Global Programs. It is a pleasure to thank Dr Cécile Penland for generously sharing her knowledge of stochastic processes and modeling, and Dr. Matthew Newman for helping to streamline the calculations performed here.

References

- Borges, M. D., and P. D. Sardeshmukh, 1995: Barotropic Rossby wave dynamics of zonally varying upper-level flows during Northern Winter. *J. Atmos. Sci.*, **52**, 3779-3796.
- Branstator, G., 1995: Organization of stormtrack anomalies by recurring low-frequency circulation anomalies. *J. Atmos. Sci.*, **52**, 207-226.
- DelSole, T., and B. F. Farrell, 1995: A stochastically excited linear system as a model for quasigeostrophic turbulence: Analytic results for one- and two- layer fluids. *J. Atmos. Sci.*, **52**, 2531-2547
- DelSole, T., 1996: Can quasi-geostrophic turbulence be modeled stochastically ?
J. Atmos. Sci., To appear. Reference will be updated.
- Farrell, B.F., 1989: Optimal excitation of baroclinic waves. *J. Atmos. Sci.*, **46**, 1193-1206.
- Frederiksen, J. S., 1983: Disturbances and eddy fluxes in Northern Hemisphere flows: Instability of three-dimensional January and July flows. *J. Atmos. Sci.*, **40**, 836-855.
- Green, J. S. A., 1977: The weather during July 1967: some dynamical considerations of the drought. *Weather*, **32**, 120-128.
- Held, I. M., S. W. Lyons, and S. Nigam, 1989: Transients and the extratropical response to El Nino. *J. Atmos. Sci.*, **46**, 163-174.

- Hoskins and Sardeshmukh, 1987: Transient eddies and the seasonal mean rotational flow. *J. Atmos. Sci.*, **44**, 328-338.
- Hoerling, M. P., and M. Ting, 1994: Organization of extratropical transients during El Nino. *J. Clim.*, **7**, 745-766.
- Kalnay, E., M. Kanamitsu, R. Kistler, W. Collins, D. Deaven, L. Gandin, M. Iredell, S. Saha, G. White, J. Woollen, Y. Zhu, M. Chelliah, W. Ebisuzaki, W. Higgins, J. Janowiak, K. C. Mo, C. Ropelewski, J. Wang, A. Leetma, R. Reynolds, R. Jenne, and D. Joseph, 1996: The NCEP/NCAR 40-Year Reanalysis Project. *Bull. Amer. Meteor. Soc.*, **77**, 437-471.
- Kok C. J., and J. D. Opsteegh, 1985: On the possible causes of anomalies in seasonal mean circulation patterns during the 1982-83 El Nino event. *J. Atmos. Sci.*, **42**, 677-694.
- Lau, N.-C., 1988: Variability of the observed midlatitude storm tracks in relation to low-frequency changes in the circulation pattern. *J. Atmos. Sci.*, **45**, 2718-2743.
- Lorenz, E., 1960: Energy and numerical weather prediction. *Tellus*, **4**, 364-373.
- Nakamura, H., and J. M. Wallace, 1990: Observed changes in baroclinic wave activity during the life cycles of low-frequency circulation anomalies. *J. Atmos. Sci.*, **47**, 1100-1116.
- Nakamura, H., 1992: Midwinter suppression of baroclinic wave activity in the Pacific. *J. Atmos. Sci.*, **49**, 1629-1642.
- Newman, M., P. D. Sardeshmukh, and C. Penland, 1995: Stochastic forcing of the wintertime extratropical flow. *J. Atmos. Sci.*, To appear. Reference will be updated.

Penland, C., 1989: Random forcing and forecasting using Principal Oscillation Pattern analysis. *Mon. Wea. Rev.*, **117**, 2165-2185.

Penland, C. and L. Matrosova, 1994: A balance condition for stochastic numerical models with applications to the El-Nino-Southern Oscillation. *J. Atmos. Sci.*, **51**, 207-226.

Penland, C. and P. D. Sardeshmukh, 1995: The optimal growth of sea surface temperature anomalies. *J. Climate*, **8**, 1999-2024.

Robertson, A. W., and W. Metz, 1989: Three-dimensional instability of persistent anomalous large-scale flows.. *J. Atmos. Sci.*, **44** , 2783-2801

Robertson, A. W., and W. Metz, 1990: Transient-eddy feedbacks derived from linear theory and observations. *J. Atmos. Sci.*, **45**, 2743-2764.

Sardeshmukh, P. D., M. Newman, and M. D. Borges, 1996: Free Rossby waves dynamics of the wintertime low-frequency flow. *J. Atmos. Sci.*, To appear. Reference will be updated.

Swartztrauber, P., 1984: Software for the spectral analysis of scalar and vector functions on the sphere. *Large Scale Scientific Computation*. Academic Press.

Valdes, P. J., and B. J. Hoskins, 1989: Linear stationary wave simulations of the time mean climatological flow. *J. Atmos. Sci.*, **46**, 2509-2527.

Wallace, J. M.; G.-H. Lim, and M. Blackmon, 1988: Relationship between cyclone tracks, anticyclone tracks and baroclinic waveguides. *J. Atmos. Sci.*, **45**, 439-462.

Figure Captions

Figure 1: Observed (a) and simulated ((b), (c) and (d)) DJF mean 400 mb high-frequency streamfunction variance. In (b), the full DJF basic state is used. In (c), only the barotropic part of the DJF mean winds are included, while in (d) only the zonally symmetric part of the barotropic winds are included. Contour interval $1 \times 10^{13} \text{ m}^4\text{s}^{-2}$ in (a) and (b), $1.125 \times 10^{12} \text{ m}^4\text{s}^{-2}$ in (c) and (d). Values greater than $6 \times 10^{13} \text{ m}^4\text{s}^{-2}$ ($6.75 \times 10^{12} \text{ m}^4\text{s}^{-2}$) are shaded in (a) and (b) ((c) and (d)). In this and all following polar stereographic plots, the outermost latitude is 10°N .

Figure 2: Observed (a) and simulated (b) DJF mean 400 mb high-frequency kinetic energy. Contour interval $15 \text{ m}^2\text{s}^{-2}$. Values greater than $90 \text{ m}^2\text{s}^{-2}$ shaded.

Figure 3: Observed (a) and simulated (b) 400 mb streamfunction tendency associated with high-frequency eddy vorticity fluxes. See text for details of computational procedure. Contour interval $3 \text{ m}^2\text{s}^{-2}$ in (a) and $6 \text{ m}^2\text{s}^{-2}$ in (b). Values less than $-3 \text{ m}^2\text{s}^{-2}$ are shaded in (a), $-6 \text{ m}^2\text{s}^{-2}$ in (b).

Figure 4: Observed (a) and simulated (b) 400 mb streamfunction tendency associated with high-frequency eddy heat fluxes. See text for details of computational procedure. Contour interval $3 \text{ m}^2\text{s}^{-2}$ in (a), values less than $-3 \text{ m}^2\text{s}^{-2}$ are shaded.

Figure 5: Observed (a) and simulated (b) 1.5 day lag covariance of DJF mean high-frequency streamfunction. Contour interval $1 \times 10^{13} \text{ m}^4\text{s}^{-2}$, values less than $-1 \times 10^{13} \text{ m}^4\text{s}^{-2}$ shaded.

Figure 6: Observed (left) and simulated (right) one-point lag correlation maps for a base point at 38.966° N , 172.5° W . Contour interval 0.1. Values less than -0.1 are shaded.

Figure 7: Observed (left) and simulated (right) one-point lag correlation maps for a base point at 46.3886° N, 63.75° E. Contour interval 0.1.

Figure 8: Maximum amplification (MA) curve for DJF basic state, together with the evolution of selected optimal perturbations. Curves are labeled with optimization time in days. Amplification factor refers to increase in total rotational kinetic energy. Extra damping included in \mathbf{D} operator is $1/10 \text{ days}^{-1}$.

Figure 9: Curve with solid circles (triangles) shows normalized ensemble mean streamfunction variance for unforced linear integrations starting from simulated (random) initial conditions. Curve with solid squares shows normalized total error variance for unforced linear integrations neglecting stochastic forcing.

Figure 10: Curve with solid circles shows pattern correlation as a function of forecast time for unforced linear integrations starting from observed high-frequency streamfunction at 400 and 800 mb. Curve with solid squares shows pattern correlation for a persistence forecast. For reference, the pattern correlation for 88 forecast (during DJF 1995/96) of 250 mb high frequency streamfunction by the operational T126 global spectral model used at NCEP are shown with open circles. See text for details.

Figure 11: Observed (left) and simulated (right) monthly mean 400 mb high frequency rotational kinetic energy for January (top) and April (bottom). Contour interval $15 \text{ m}^2\text{s}^{-2}$, with values greater than $105 \text{ m}^2\text{s}^{-2}$ are shaded.

Figure 12: Observed (a) and simulated (b) standard deviation of DJF mean 400 mb high frequency streamfunction variance for 13 winters (DJF 1982/83 to 1994/95). Individual winter means were

truncated to T12 resolution before standard deviation was computed. Contour interval is $2 \times 10^{12} \text{ m}^4 \text{ s}^{-2}$, values greater than $1.2 \times 10^{13} \text{ m}^4 \text{ s}^{-2}$ are shaded.

Figure 13: Observed (left) and simulated (right) anomalous DJF mean 400 mb high-frequency streamfunction variance for three selected winters. Fields are truncated to T12 resolution. Contour interval is $3 \times 10^{12} \text{ m}^4 \text{ s}^{-2}$, values less than $-3 \times 10^{12} \text{ m}^4 \text{ s}^{-2}$ are shaded. Anomalies are computed relative to 13 winter mean (DJF 1982/83 to 1994/95). Anomaly correlation (AC) between observed and simulated fields is indicated.

Figure 14: Simulated DJF mean 400 mb high-frequency rotational kinetic energy computed from FDR with stochastic forcing that is white in both space and time in (a) the kinetic energy and (b) the vorticity norms. Contour interval $15 \text{ m}^2 \text{ s}^{-2}$. Values greater than $90 \text{ m}^2 \text{ s}^{-2}$ shaded.

Figure 15: (a) Map of stochastic forcing variance at 400 mb (the diagonal elements of \mathbf{Q} displayed in grid space). \mathbf{Q} computed using observed streamfunction covariance matrix (\mathbf{C}_0) via the backward FDR, and truncated to be positive definite. Contour interval $1200 \text{ m}^2 \text{ s}^{-2}$, values greater than $6200 \text{ m}^2 \text{ s}^{-2}$ shaded (b) Streamfunction variance calculated from solution of the FDR using this \mathbf{Q} . Contour interval $1 \times 10^{13} \text{ m}^4 \text{ s}^{-2}$, values greater than $6 \times 10^{12} \text{ m}^4 \text{ s}^{-2}$ shaded.

Figure 16: $\text{Tr}(\mathbf{C}_0)$ (solid circles) and leading eigenvalue of \mathbf{C}_0 (solid squares) as a function of damping time scale of the \mathbf{D} operator. Leading eigenvalue of the covariance matrix expressed as percent variance explained by the first eigenvector. \mathbf{C}_0 is calculated by the solving the FDR (7a) with the scaling parameter ϵ chosen so that $\text{Tr}\mathbf{Q} = \mathbf{I}$.

Table Captions

Table 1: Summary of results of calculations for individual winter seasons. AC is correlation between observed and simulated T12 anomalous high-frequency 400 mb streamfunction variance. Anomalies are computed related to the 13 winter mean. Extra damping included in \mathbf{D} operator for each DJF mean basic state is such that the least damped eigenmode of \mathbf{B} is damped with an e-folding time scale of 20 days. See text for further details.

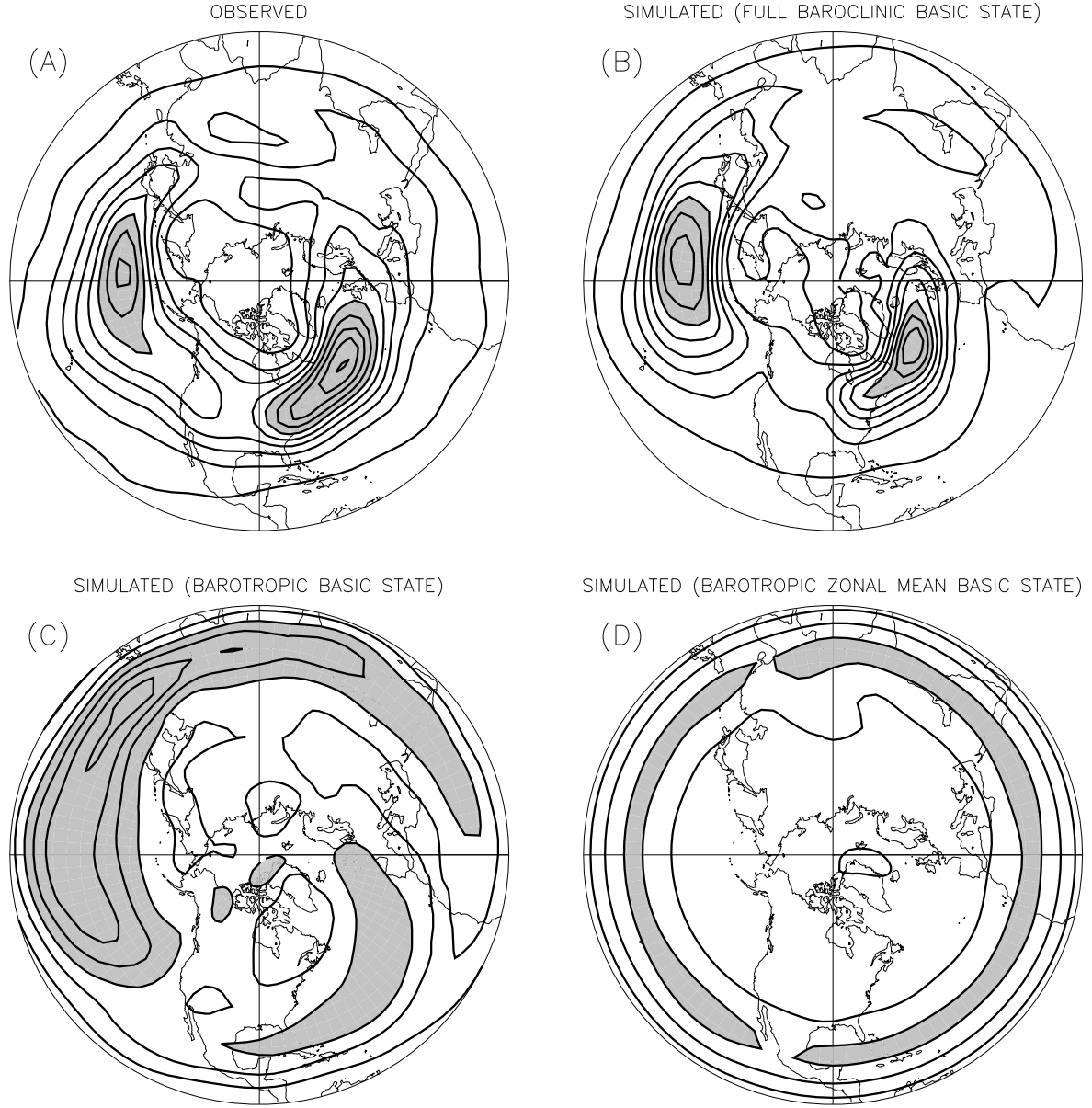


Figure 1: Observed (a) and simulated ((b),(c) and (d)) DJF mean 400 mb high-frequency streamfunction variance. In (b), the full DJF basic state is used. In (c), only the barotropic part of the DJF mean winds are included, while in (d) only the zonally symmetric part of the barotropic winds are included. Contour interval $1 \times 10^{13} \text{ m}^4 \text{ s}^{-2}$ in (a) and (b), $1.125 \times 10^{13} \text{ m}^4 \text{ s}^{-2}$ in (c) and (d). Values greater than $6 \times 10^{13} \text{ m}^4 \text{ s}^{-2}$ ($6.75 \times 10^{12} \text{ m}^4 \text{ s}^{-2}$) are shaded in (a) and (b) ((c) and (d)). In this and all following polar stereographic plots, the outermost latitude is 10°N .

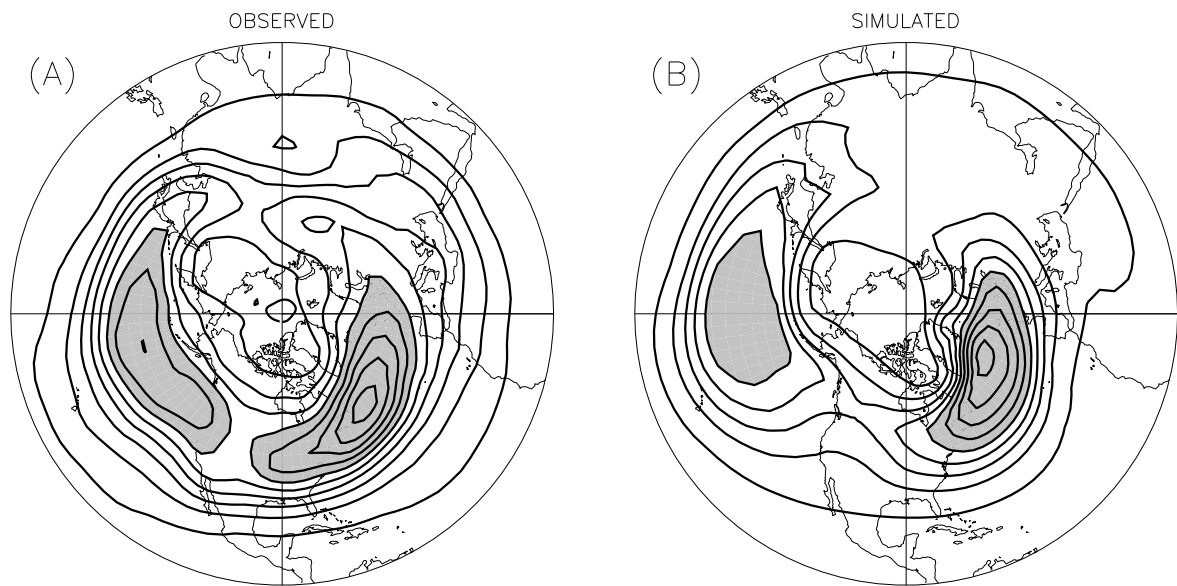


Figure 2: Observed (a) and simulated (b) DJF mean 400 mb high-frequency rotational kinetic energy. Contour interval 15 $\text{m}^2 \text{s}^{-2}$. Values greater than 90 $\text{m}^2 \text{s}^{-2}$ shaded.

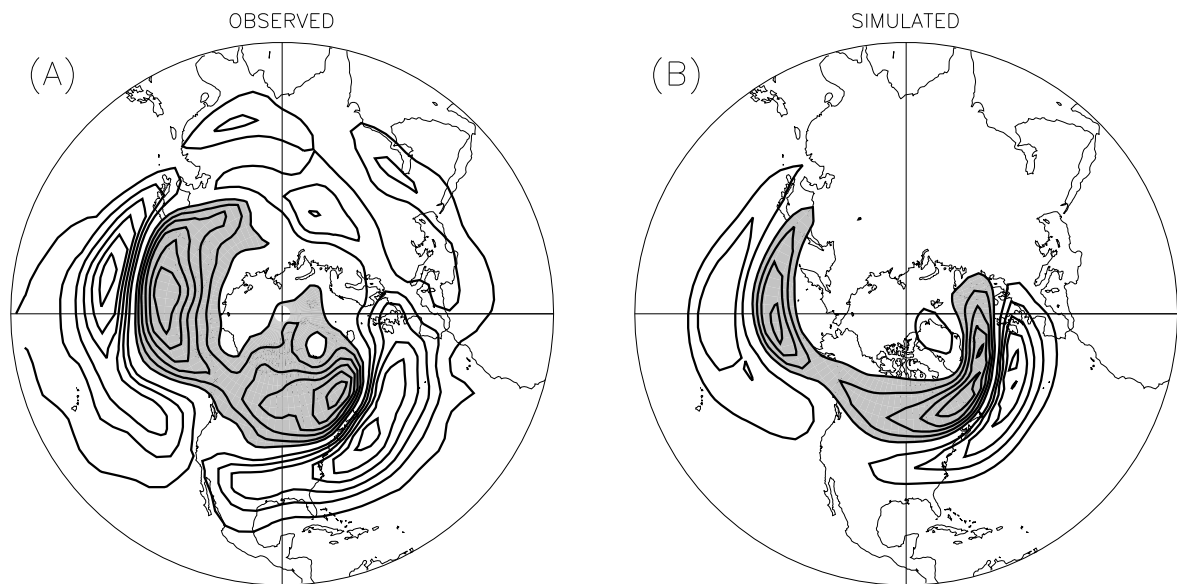


Figure 3: Observed (a) and simulated (b) DJF mean 400 mb streamfunction tendency associated with high-frequency eddy vorticity fluxes. See text for details of computational procedure. Contour interval $3 \text{ m}^2 \text{ s}^{-2}$ in (a) and $6 \text{ m}^2 \text{ s}^{-2}$ in (b). Values less than $-3 \text{ m}^2 \text{ s}^{-2}$ shaded in (a), $-6 \text{ m}^2 \text{ s}^{-2}$ in (b).

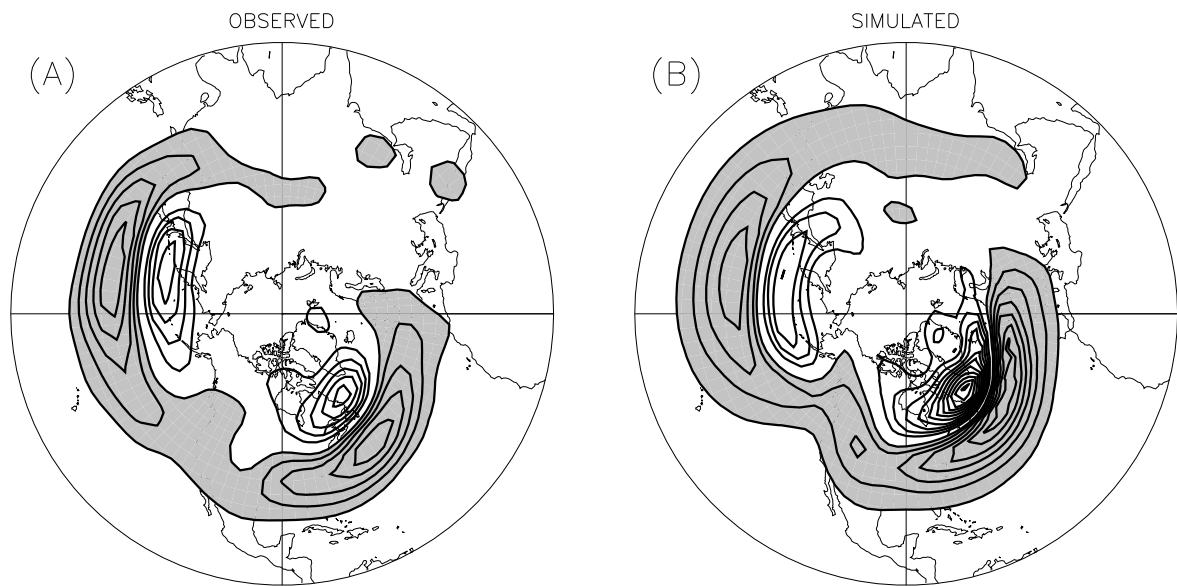


Figure 4: Observed (a) and simulated (b) DJF mean 400 mb streamfunction tendency associated with high-frequency eddy heat fluxes. See text for details of computational procedure. Contour interval $3 \text{ m}^2 \text{ s}^{-2}$, values less than $-3 \text{ m}^2 \text{ s}^{-2}$ shaded.

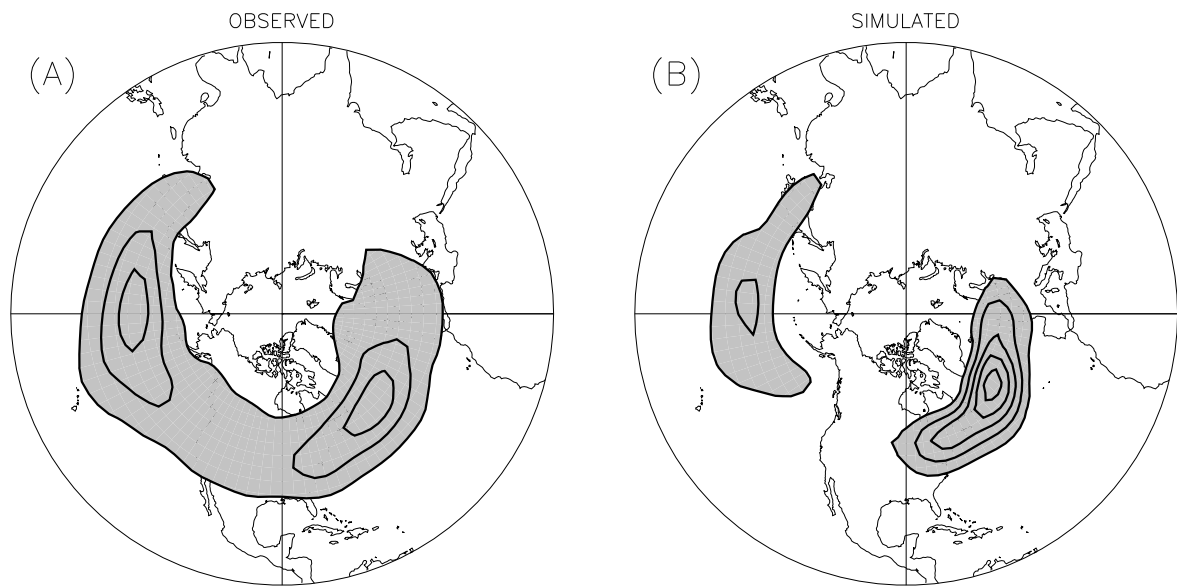


Figure 5: Observed (a) and simulated (b) 1.5 day lag covariance of DJF mean 400 mb high-frequency streamfunction. Contour interval $1 \times 10^{13} \text{ m}^4 \text{ s}^{-2}$, values less than $-1 \times 10^{13} \text{ m}^4 \text{ s}^{-2}$ shaded.

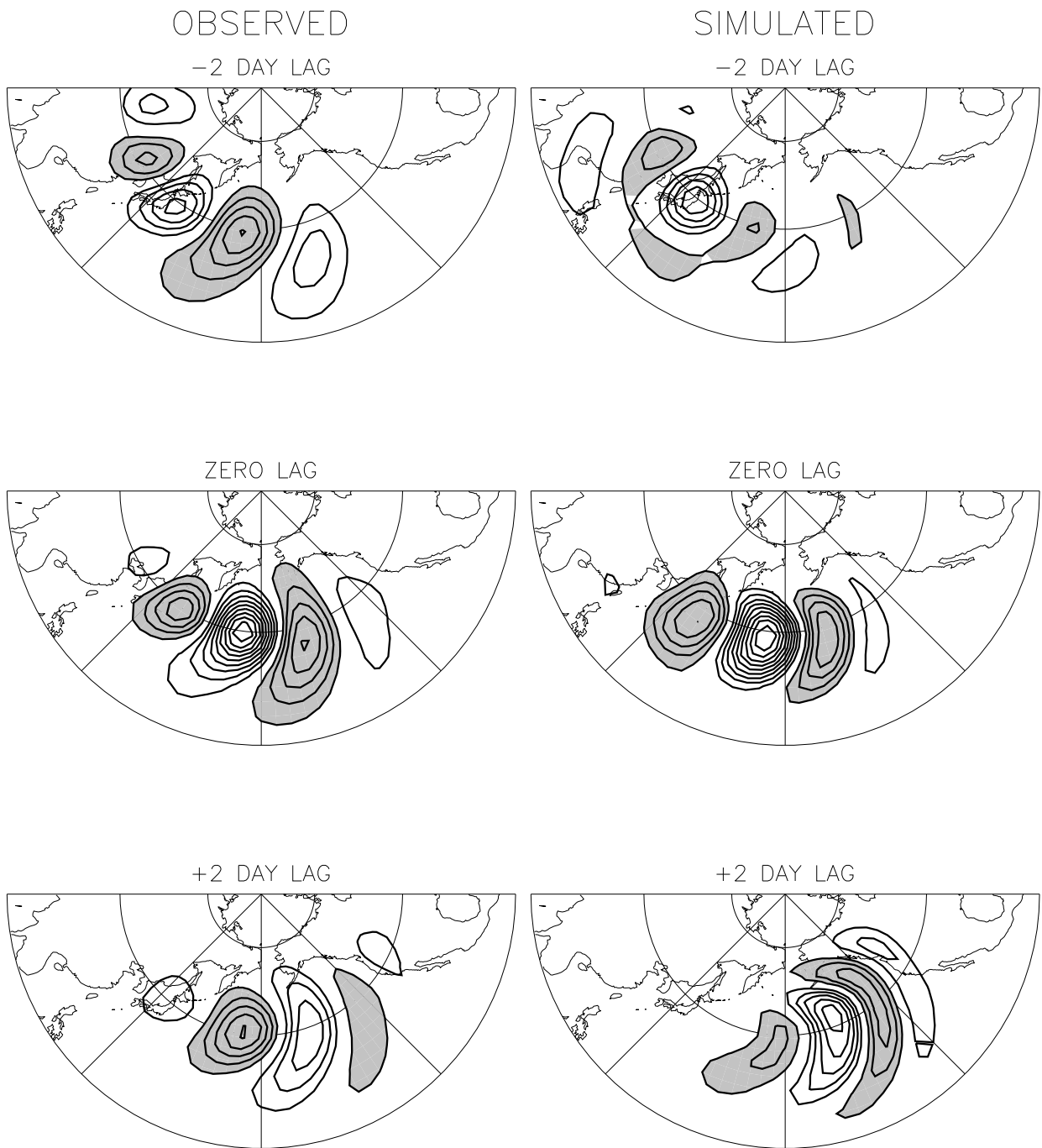


Figure 6: Observed (left) and simulated (right) one-point lag correlation maps for a base point at 38.966 °N, 172.5 °W. Contour interval is 0.1. Values less than -0.1 are shaded.

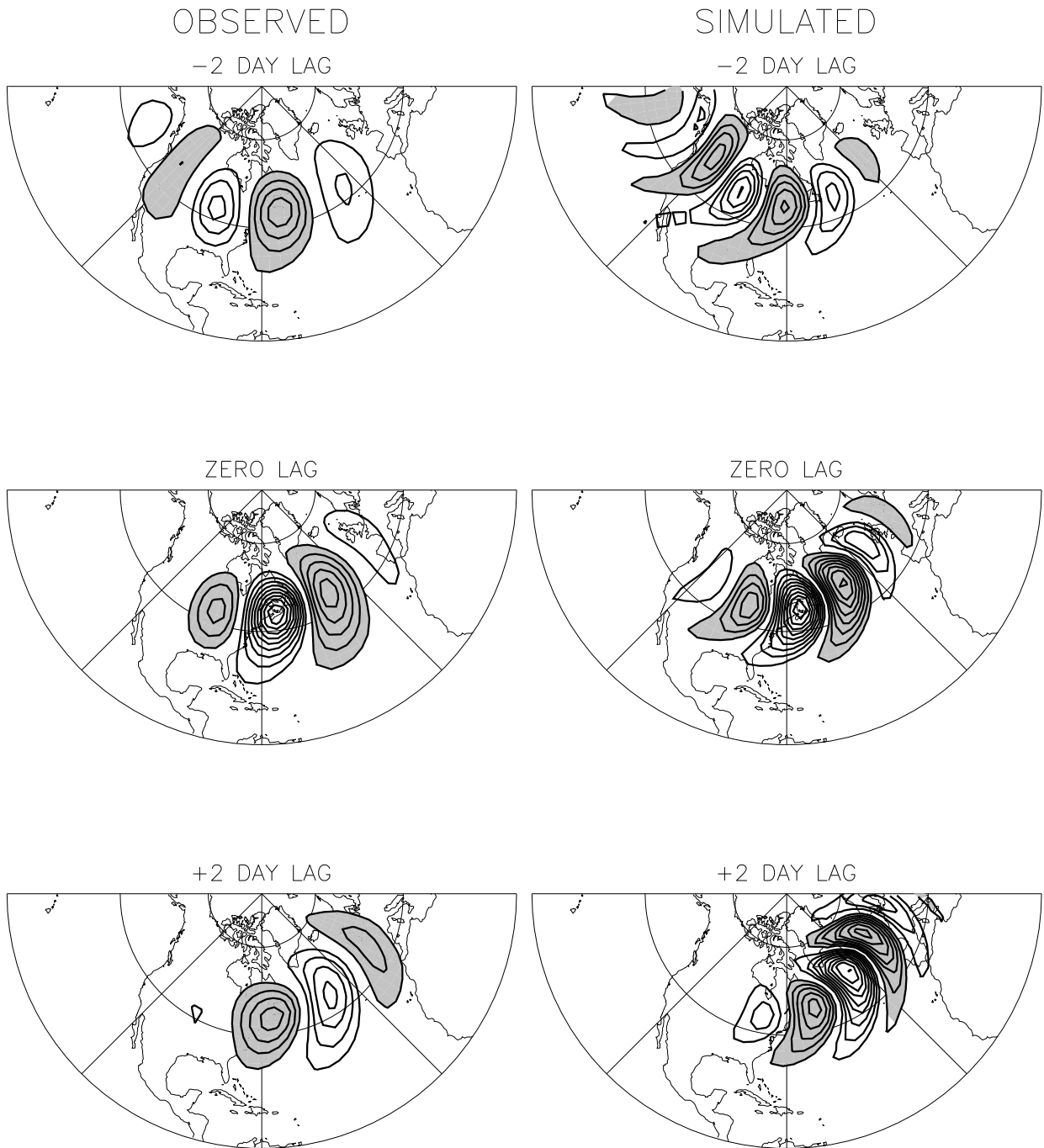


Figure 7: Observed (left) and simulated (right) one-point lag correlation maps for a base point at 46.3886 °N, 63.75 °E. Contour interval is 0.1. Values less than -0.1 are shaded.

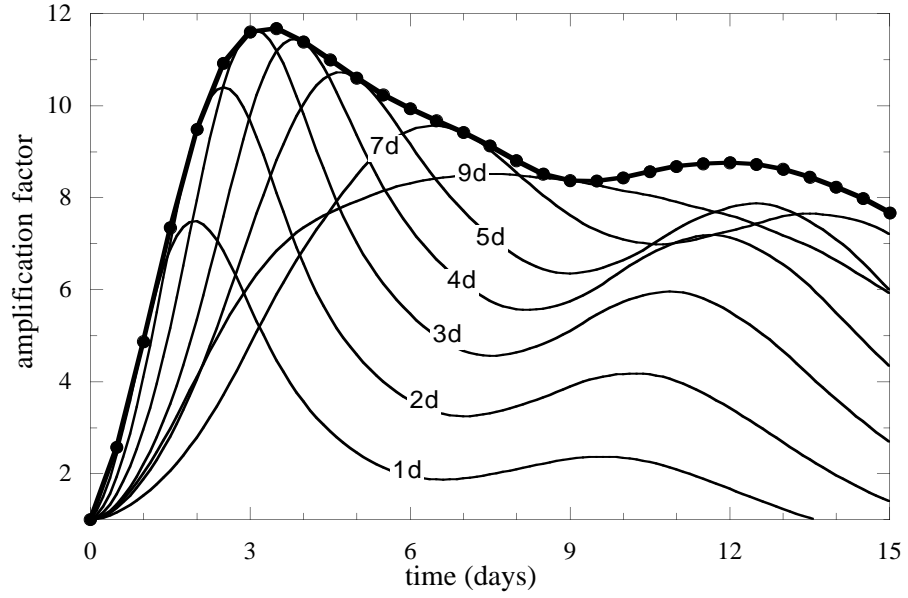


Figure 8: Maximum amplification (MA) curve for DJF basic state, together with the evolution of selected optimal perturbations. Curves are labelled with optimization time in days. Amplification factor refers to increase in total rotational kinetic energy. Extra damping included in \mathbf{D} operator is $1/10 \text{ days}^{-1}$.

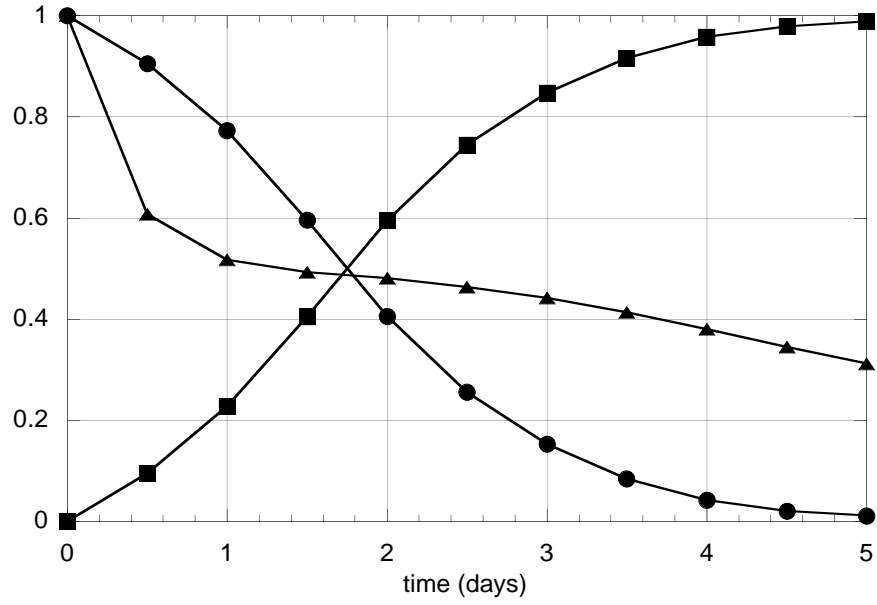


Figure 9: Curve with solid circles (triangles) shows normalized ensemble mean stream-function variance for unforced linear integrations starting from observed (random) initial conditions. Curve with solid squares shows normalized error variance for unforced linear integrations neglecting stochastic forcing. See text for details.

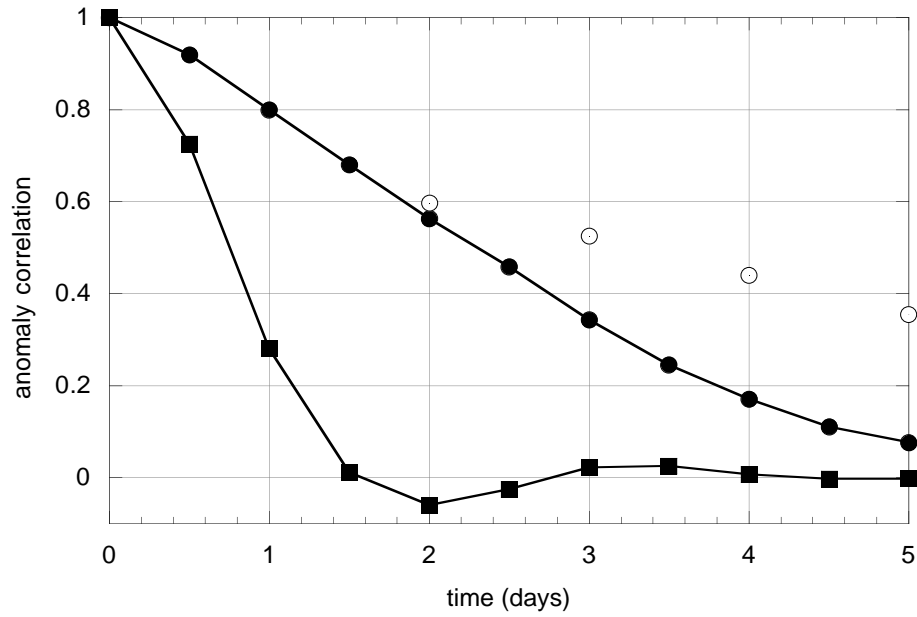


Figure 10: Curve with solid circles shows anomaly correlation (AC) as a function of forecast time for unforced linear integrations starting from observed high-frequency streamfunction at 400 and 800 mb. Curve with solid squares shows AC for a persistence forecast. For reference, the AC for 88 forecasts (during DJF 1995/96) of 250 mb high-frequency streamfunction by the operational T126 global spectral model used at NCEP are shown with open circles.

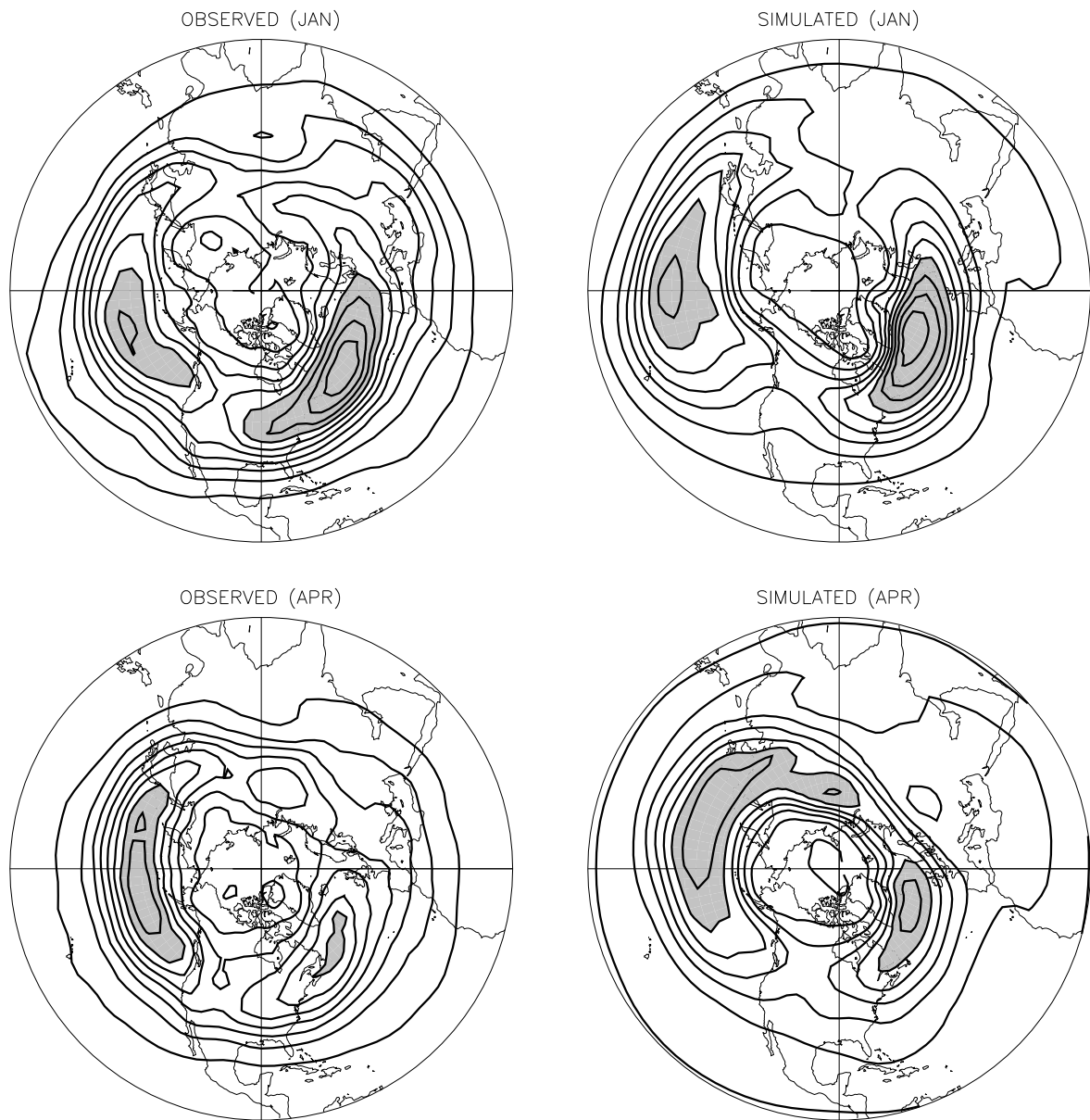


Figure 11: Observed (left) and simulated (right) monthly mean 400 mb high-frequency rotational kinetic energy for January (top) and April (bottom). Contour interval $15 \text{ m}^2 \text{ s}^{-2}$, with values greater than $105 \text{ m}^2 \text{ s}^{-2}$ shaded.

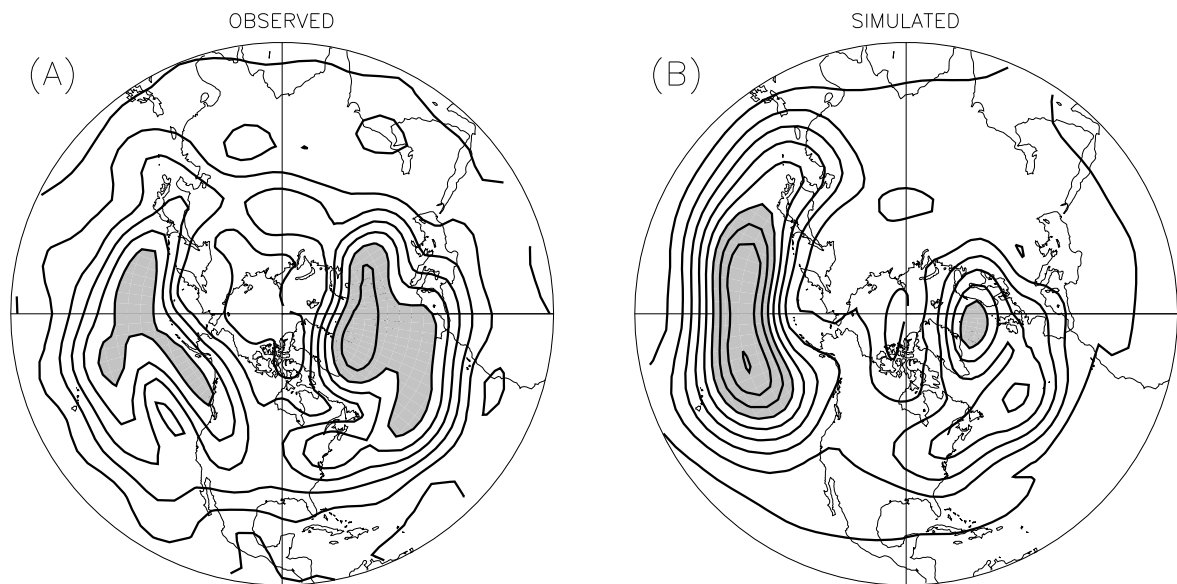


Figure 12: Observed (A) and simulated (B) standard deviation of DJF mean 400 mb high-frequency streamfunction variance for 13 winters (DJF 1982/83 to 1994/95). Individual winter means were truncated to T12 resolution before standard deviation was computed. Contour interval is $2 \times 10^{12} \text{ m}^4 \text{ s}^{-2}$, values greater than $1.2 \times 10^{13} \text{ m}^4 \text{ s}^{-2}$ are shaded.

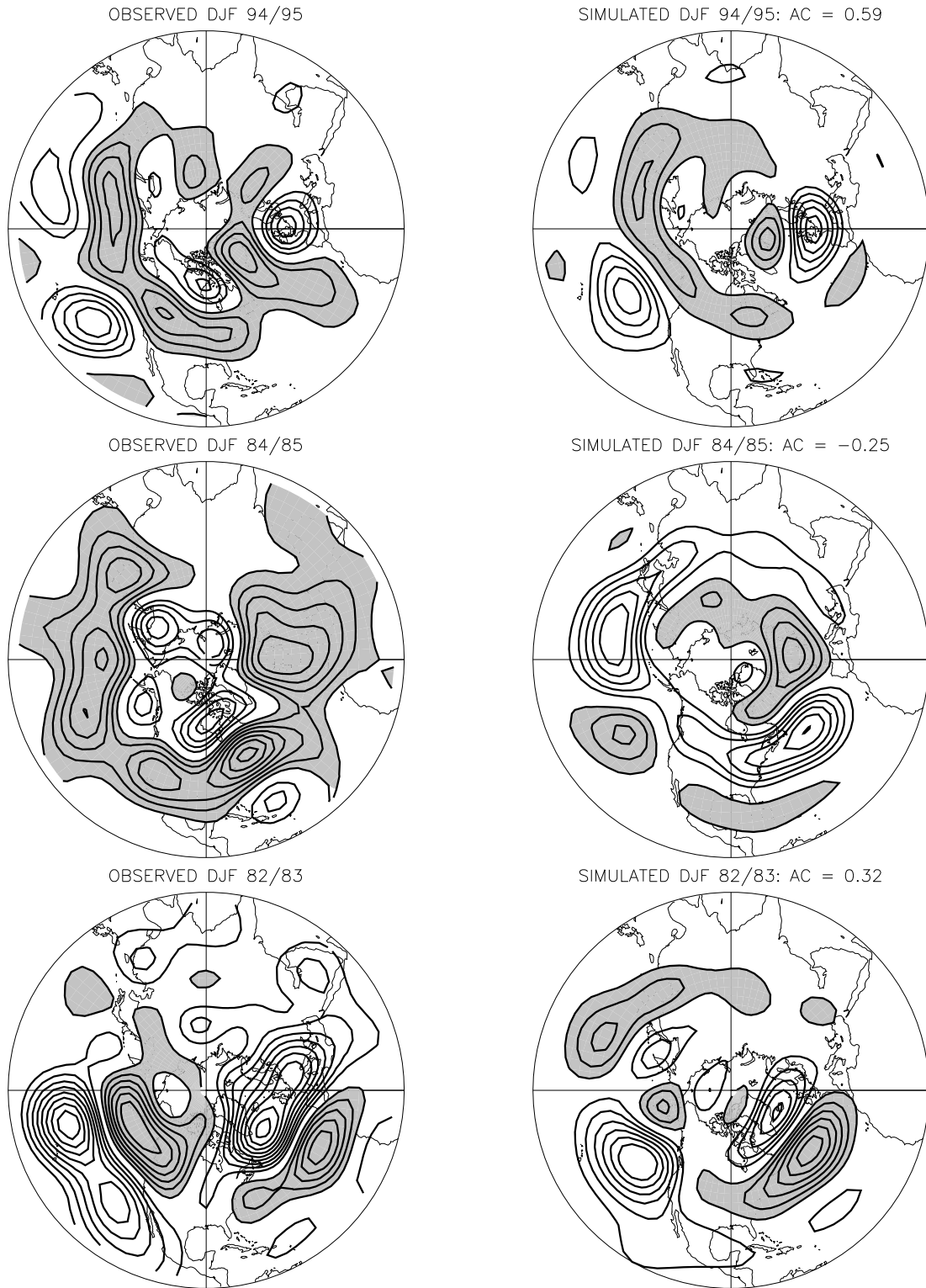


Figure 13: Observed (left) and simulated (right) anomalous DJF mean 400 mb high-frequency streamfunction variance for three selected winters. Fields are truncated to T12 resolution. Contour interval is $3 \times 10^{12} \text{ m}^4 \text{ s}^{-2}$, values less than $-3 \times 10^{12} \text{ m}^4 \text{ s}^{-2}$ are shaded. Anomalies are computed relative to 13 winter mean (DJF 1982/83 to 1994/95). Pattern correlation between observed and simulated anomalies (AC) is indicated.

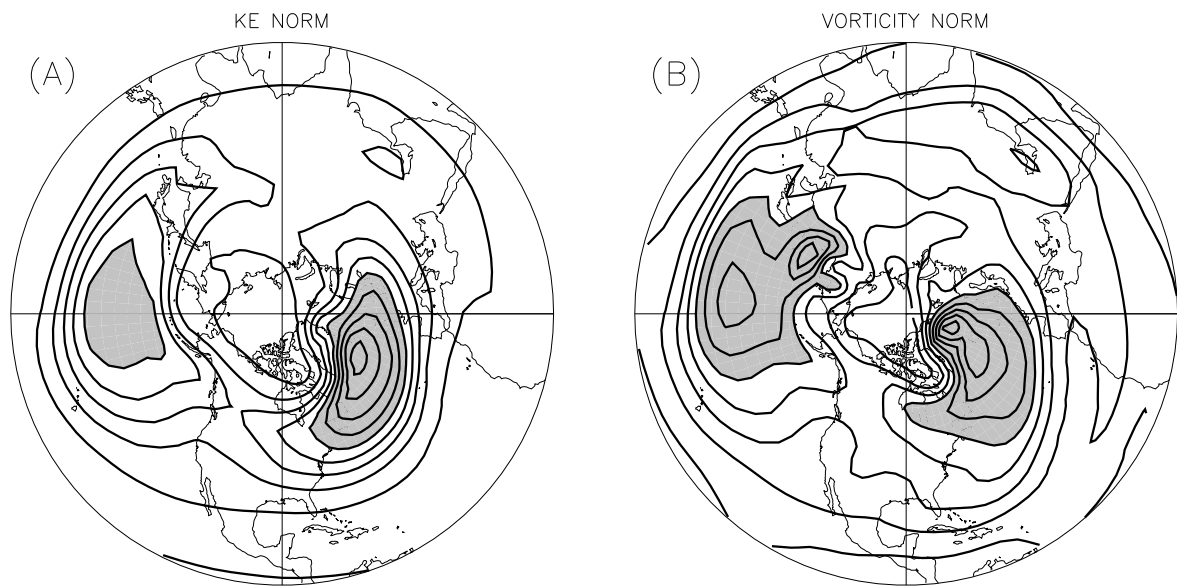


Figure 14: Simulated DJF mean 400 mb high-frequency rotational kinetic energy computed from the FDR with stochastic forcing that is white in both space and time in (a) the rotational kinetic energy norm and (b) the vorticity norm. Contour interval $15 \text{ m}^2 \text{ s}^{-2}$, values greater than $90 \text{ m}^2 \text{ s}^{-2}$ are shaded.

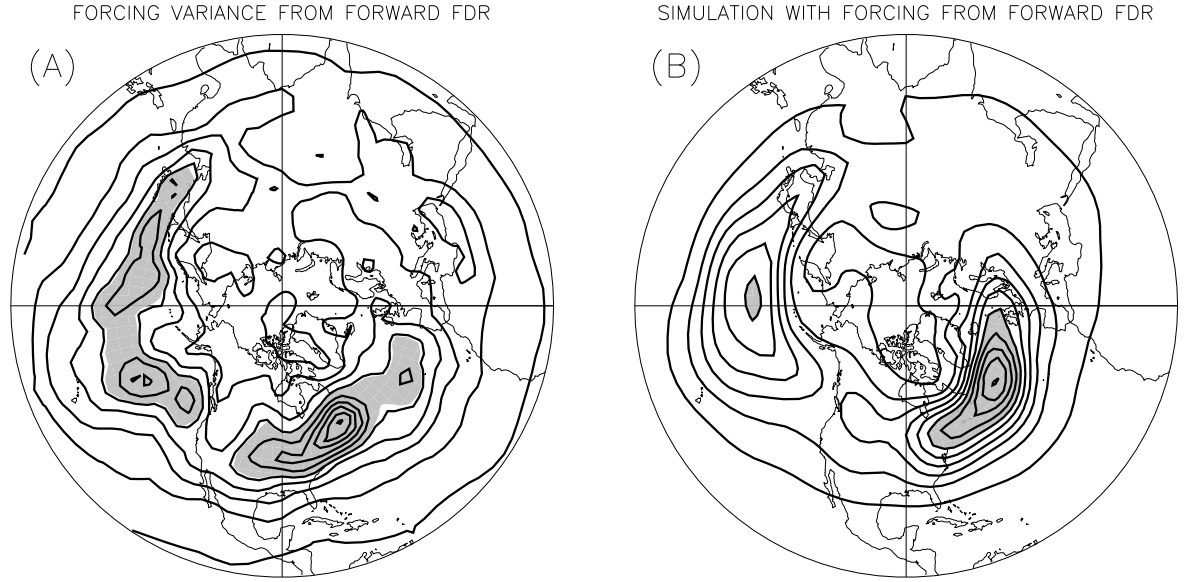


Figure 15: (a) Map of stochastic forcing variance at 400 mb. Stochastic forcing computed from forward FDR (equation (7)), using observed high-frequency streamfunction covariance matrix. Contour interval $1200 \text{ m}^4 \text{ s}^{-4}$, values greater than $6200 \text{ m}^4 \text{ s}^{-4}$ are shaded. (b) Simulated 400 mb high-frequency streamfunction variance from solution of the FDR using forcing covariance matrix shown in (a). Contour interval is $1 \times 10^{13} \text{ m}^4 \text{ s}^{-2}$, values greater than $6 \times 10^{13} \text{ m}^4 \text{ s}^{-2}$ are shaded.

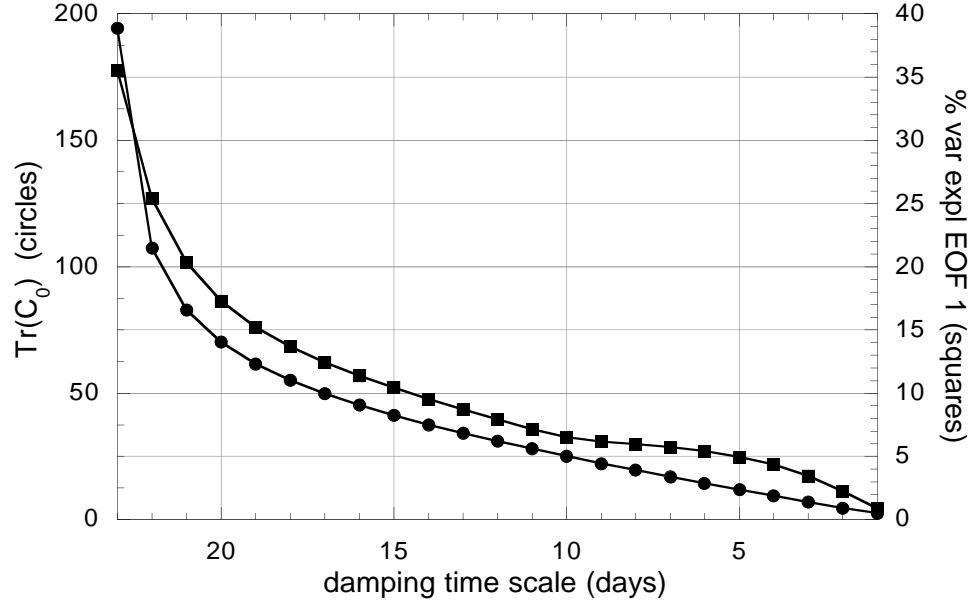


Figure 16: Trace of \mathbf{C}_0 (solid circles) and leading eigenvalue of \mathbf{C}_0 (solid squares) as a function of damping time scale of the \mathbf{D} operator. Leading eigenvalue of the covariance matrix (\mathbf{C}_0) is expressed as percent variance explained by the first eigenvector. \mathbf{C}_0 is calculated by solving the FDR (7a) with the scaling parameter ϵ chosen so that $Tr\mathbf{Q} = 1$.

winter of	AC
82/83	0.32
83/84	0.08
84/85	-0.25
85/86	-0.17
86/87	0.33
87/88	0.46
88/89	0.08
89/90	0.45
90/91	0.22
91/92	0.24
92/93	0.50
93/94	0.18
94/95	0.59

Table 1: Summary of results of calculations for individual winter seasons. AC is pattern correlation between observed and simulated T12 anomalous high-frequency 400 mb streamfunction variance. Anomalies are computed relative to 13 winter mean. Extra damping included in *D* operator for each DJF mean basic state is such that least damped eigenmode of *B* is damped with an e-folding time scale of 20 days. See text for further details.